



Durham Research Online

Deposited in DRO:

16 July 2019

Version of attached file:

Published Version

Peer-review status of attached file:

Peer-reviewed

Citation for published item:

Devi, N. Chandrachani and Rodríguez-Puebla, Aldo and Valenzuela, O. and Avila-Reese, Vladimir and Hernández-Aguayo, César and Li, Baojiu (2019) 'The galaxy halo connection in modified gravity cosmologies : environment dependence of galaxy luminosity function.', *Monthly notices of the Royal Astronomical Society.*, 488 (1). pp. 782-802.

Further information on publisher's website:

<https://doi.org/10.1093/mnras/stz1664>

Publisher's copyright statement:

© 2019 The Author(s). Published by Oxford University Press on behalf of the Royal Astronomical Society.

Additional information:

Use policy

The full-text may be used and/or reproduced, and given to third parties in any format or medium, without prior permission or charge, for personal research or study, educational, or not-for-profit purposes provided that:

- a full bibliographic reference is made to the original source
- a [link](#) is made to the metadata record in DRO
- the full-text is not changed in any way

The full-text must not be sold in any format or medium without the formal permission of the copyright holders.

Please consult the [full DRO policy](#) for further details.

The galaxy–halo connection in modified gravity cosmologies: environment dependence of galaxy luminosity function

N. Chandrachani Devi^{1,2★}, Aldo Rodríguez-Puebla,¹ O. Valenzuela,¹
Vladimir Avila-Reese,¹ César Hernández-Aguayo³ and Baojiu Li³

¹*Instituto de Astronomía, Universidad Nacional Autónoma de México, A. P. 70-264, 04510 México, D.F., México*

²*Instituto de Física, Universidad Nacional Autónoma de México, Circuito de la Investigación Científica Ciudad Universitaria, 04510 México, D.F., México*

³*Institute for Computational Cosmology, Department of Physics, Durham University, South Road, Durham DH1 3LE, UK*

Accepted 2019 June 10. Received 2019 May 22; in original form 2019 January 4

ABSTRACT

We investigate the dependence of the galaxy–halo connection and galaxy density field in modified gravity models using the N -body simulations for $f(R)$ and nDGP models at $z = 0$. Because of the screening mechanisms employed by these models, chameleon and Vainshtein, haloes are clustered differently in the non-linear regime of structure formation. We quantify their deviations in the galaxy density field from the standard Λ cold dark matter (Λ CDM) model under different environments. We populate galaxies in haloes via the (sub)halo abundance matching. Our main results are as follows: (1) The galaxy–halo connection *strongly* depends on the gravity model; a maximum variation of ~ 40 per cent is observed between halo occupational distribution (HOD) parameters; (2) $f(R)$ gravity models predict an excess of galaxies in low-density environments of ~ 10 per cent but predict a deficit of ~ 10 per cent at high-density environments for $|f_{R0}| = 10^{-4}$ and 10^{-6} while $|f_{R0}| = 10^{-5}$ predicts more high-density structures; nDGP models are consistent with Λ CDM; (3) different gravity models predict different dependences of the galaxy luminosity function (GLF) with the environment, especially in void-like regions we find differences around ~ 10 per cent for the $f(R)$ models while nDPG models remain closer to Λ CDM for low-luminosity galaxies but there is a deficit of ~ 11 per cent for high-luminosity galaxies in all environments. We conclude that the dependence of the GLF with environment might provide a test to distinguish between gravity models and their screening mechanisms from the Λ CDM. We provide HOD parameters for the gravity models analysed in this paper.

Key words: galaxies: haloes – dark energy – dark matter – large-scale structure of Universe.

1 INTRODUCTION

The standard model of cosmology assumes that our Universe is homogeneous and isotropic and that our current knowledge of gravity is well described by general relativity (GR). With the recent discovery of the late-time accelerated expansion (Riess et al. 1998; Perlmutter et al. 1999), the most popular approach to describe the dynamics of our Universe within the general relativity framework is by introducing the hypothesis of a dark energy component with a negative pressure permeating all over the space. Among the various explanations proposed, there are mainly two candidates for dark energy well studied in literature. One are quintessence models in which the dark energy is governed by a dynamical scalar field (Ratra & Peebles 1988). The other candidate is the cosmological

constant Λ , incarnated as a vacuum energy that remains after the inflationary epoch (for a review see Carroll 2001). Yet the Λ cold dark matter model, Λ CDM, remains as the most popular and widely accepted cosmological gravity model.

The Λ CDM model is highly successful in explaining a number of cosmological probes such as the temperature anisotropies and polarization in the cosmic microwave background radiation (CMBR), the baryon acoustic oscillations (BAOs) imprinted in the Galaxy spatial distributions at large scales, and the accelerated expansion inferred mainly from observations of high-redshift Type Ia supernovae (Planck Collaboration XIII 2016; Planck collaboration VI 2018). The Λ CDM model provides also a successful background to explain a number of astronomical observations such as the galaxy clustering for both local and high-redshift galaxies (e.g. Conroy, Wechsler & Kravtsov 2006; Reddick et al. 2013, see for a review, Frenk & White 2012), the galaxy cluster mass function (e.g. Vikhlinin et al. 2009), the so-called star-forming main sequence of Galaxies at different

* E-mail: chandrachani@gmail.com

redshifts (e.g. Behroozi, Wechsler & Conroy 2013b; Rodríguez-Puebla et al. 2016b), and a number of galaxy demographics and relationships that have been well studied based on analytic and semi-analytic models (e.g. Mo, Mao & White 1998; Firmani & Avila-Reese 2000; Baugh 2006) and large cosmological hydrodynamics simulations (Vogelsberger et al. 2014; Schaye et al. 2015) of galaxy formation (for a review, see Somerville & Davé 2015, and more references therein).

Despite of the success of the Λ CDM cosmology, so far, we do not have a solution to the problems that raises the explanation of the origin of Λ (Weinberg 1989; Sahni & Starobinsky 2000), nor GR has been tested on cosmological scales, though there are some hints of being valid at galactic scales (Collett et al. 2018). In addition, the recently reported $\sim 3.5\sigma$ discrepancy between the Hubble constant, H_0 , locally determined (Beaton et al. 2016; Freedman 2017; Riess et al. 2018) and the one estimated from the CMBR anisotropies (Planck Collaboration XIII 2016; Planck Collaboration VI 2018), has led to a tension within the standard cosmology (Riess et al. 2016); but see Shanks, Hogarth & Metcalfe (2019) for a possible solution for the above tension and Riess et al. (2018) for a counterargument to that paper. The above has been interpreted as the necessity to consider a revision of our knowledge on gravity over cosmological scales or perhaps new physics.

1.1 Modified gravity models and their screening mechanisms

Recently, alternative modified gravity (MG) models have received a lot of attention as they offer interesting and possible alternative explanations to the cosmic acceleration of the Universe, without invoking dark energy but by naturally modifying GR on cosmological scales. None the less, even when these models are modification to GR on the large scales, they still need to satisfy the tight constraints on deviations from GR from the Solar system (Will 2014). Screening mechanisms have helped to overcome the potential inconsistency; some of them were developed with the aim to suppress efficiently the fields that mediate the MG force at small scales while enhancing the effect of gravity over cosmological scales (Vainshtein models) or at scales smaller than the scalar field Compton wavelength (Khoury 2010; Joyce et al. 2015).

In this work, we will explore two types of MG models: the normal Dvali, Gabadadze & Porrati (2000) (DGP) model and the chameleon $f(R)$ model (Hu & Sawicki 2007). The former assumes that the standard model of particles live in a 4D spacetime brane embedded within a higher dimensional 5D space in which only gravity propagates. The latter introduces an arbitrary function of the Ricci scalar that generalizes the Einstein–Hilbert action; here, we consider the functional form proposed by Hu & Sawicki (2007). While there are several other classes of MG models, we explore here only the above two models as they are the most popular and widely studied proposals so far (for a review see Koyama 2016).

As for the screening mechanisms, there are two types well studied, the Vainshtein and the chameleon ones. In this work, the former is applied to the DGP model and the latter to the $f(R)$ model. In both models, the screening mechanism is governed by an extra degree of freedom introduced, most of the time, as a scalar field that follows a non-linear equation strongly coupled to the density field. As a result, one expects that the clustering of the dark matter particles is different between these two screening mechanisms; the Vainshtein mechanism depends on the locations of the particles in the cosmic web while in chameleon mechanism is roughly independent (Falck, Koyama & Zhao 2015). This leads to the speculation that screening mechanisms might affect the structure

and spatial distribution of dark matter haloes. Indeed, recent studies have shown that screening mechanisms affect haloes differently. Based on high-resolution N -body simulations Falck et al. (2015) showed that the Vainshtein screening mechanism is independent of halo mass and is very efficient inside the virial radius but decreases at larger radii. Instead, the chameleon mechanism depends on halo mass and the strength of f_{R0} , as well as on halo screening profiles; for similar conclusions see (Zhao, Li & Koyama 2011; Winther, Mota & Li 2012; Shi, Li & Han 2017). Thus, it is of interest to see whether such effects can be detected observationally in the correlations and statistical distributions of galaxies and cluster of galaxies.

1.2 Exploring the effects of MG models on the galaxy distributions

Based on the discussion above, we propose to study here the galaxy density field under the $f(R)$ and DGP MG models and their respective screening mechanisms. Galaxies are biased tracers of dark matter haloes, and dark matter haloes are biased tracers of the dark matter particles distribution. The latter is due to the highly non-linear evolution of the mass density perturbation field, and the former is consequence of the complex gastro-physical processes that govern galaxy formation and evolution (Somerville & Davé 2015). While galaxy formation within the evolving dark matter haloes remains as one of the most challenging problems in modern astronomy, the statistical matching between observed galaxies and simulated dark matter haloes allows for a direct connection of galaxies to haloes. This connection has been very well constrained in the past not only for local galaxies but up to very high redshifts (see e.g. Rodríguez-Puebla et al. 2017; Behroozi et al. 2018; for a recent review, see Wechsler & Tinker 2018). Thus, the results from N -body simulations of structure formation under MG cosmologies can be connected statistically to galaxies, in such a way that the measured galaxy correlations and spatial distributions in the simulations can be compared with observations.

Using galaxies to constrain MG models is not a new idea (Koyama 2016, see for a review of various astrophysical test using galaxies). Indeed, present and future spectroscopic and imaging galaxy surveys, such as the extended Baryon Oscillation Spectroscopic Survey (eBOSS),¹ the dark energy survey (DES),² the Dark Energy Spectroscopic Instrument (DESI)³ (Aghamousa et al. 2016), and the European Space Agency’s-Euclid⁴ not only will allow to test the gravity theory on the largest scales of our Universe but also will allow to constrain a wide range of cosmological scenarios.

The main goal of this work is to quantify the effects of the different gravity models discussed above on the statistics of the dark matter haloes, and its implication on the distributions of their host galaxies.

In particular, we will do so by studying their density field via the galaxy luminosity function (GLF) at $z \approx 0$, when the effects of environments are more relevant. This way, we will evaluate whether observational tests, as the variation of the GLF with environment, could be useful for discriminating the studied MG models.

In this paper, we generate galaxy mock catalogues using N -body simulations via the (sub)halo abundance matching (SHAM) technique. We will focus mainly on the results based on the GLF

¹<https://www.sdss.org/surveys/eboss/>

²<https://www.darkenergysurvey.org/es/>

³<https://www.desi.lbl.gov/>

⁴<https://www.euclid-ec.org/>

in the r band and its dependence on large-scale environment. The viability of our mock catalogues is tested by showing that all the models produce two-point correlation function that are in agreement with the observations from the SDSS DR7 (Zehavi et al. 2011). We also provide halo occupational distribution (HOD) parameters for all our galaxy mocks based on different MG models.

This paper is organized as follows. In Section 2, we describe the MG models we employed: $f(R)$ and DGP models. In Section 3 we describe the suite of simulations we use for the MG models, previously described in Li et al. (2012) and Li, Zhao & Koyama (2013). Section 4 describes the SHAM approach we use for the galaxy–halo connection and we show that all our galaxy mocks produce realistic two-point correlation function. In Section 5 we present our results on the predicted galaxy density field and the dependence of the GLF with environment. In Section 6 we discuss our results. Finally, Section 7 we present a summary with our main results and a discussion.

The cosmological parameters used for this paper are: $\Omega_m = 0.281$, $\Omega_\Lambda = 1 - \Omega_m$, $n_s = 0.971$, and $\sigma_8 = 0.820$.

2 MODIFIED GRAVITY MODELS

In this section, we briefly describe the two models of MG that we will use in this paper.

2.1 $f(R)$ gravity model

First, we consider the $f(R)$ theories of gravity, where the Ricci scalar R in the Einstein–Hilbert action is generalized by a functional form $f(R)$:

$$S = \frac{1}{2\kappa} \int d^4x \sqrt{-g} (R + f(R)) + S_m(g_{\mu\nu}, \psi_m), \quad (1)$$

where $\kappa = 8\pi G$, G is the Newtonian gravitational constant, g is the determinant of the metric tensor $g_{\mu\nu}$, $f(R)$ is an arbitrary function of the Ricci scalar R , and S_m is the matter action that depends on $g_{\mu\nu}$ and matter fields ψ_m .

By varying the action with respect to the metric $g_{\mu\nu}$, we obtain the modified Einstein equations (De Felice & Tsujikawa 2010)

$$f_R(R)R_{\mu\nu} - \frac{1}{2}f(R)g_{\mu\nu} - \nabla_\mu \nabla_\nu f_R(R) + g_{\mu\nu} \square f_R(R) = \kappa T_{\mu\nu}, \quad (2)$$

where $f_R(R) = df(R)/dR$ represents the extra degree of freedom, i.e. the scalar field and often known as the scalaron field. The d’Alembertian operator is denoted with $\square = \nabla_\alpha \nabla^\alpha$ and ∇_α is the usual covariant derivative associated with respect to the affine connections of the metric while $T_{\mu\nu}$ is the energy–momentum tensor of the matter fields.

Thus, under the scalar field representation of $f(R)$, the equation of motion that determines the dynamics of scalar field, f_R , is given by the trace of equation (1)

$$\square f_R = \frac{1}{3} [R - f_R R + 2f(R) - 8\pi G \rho_m] = \frac{\partial V_{\text{eff}}}{\partial f_R}. \quad (3)$$

Here ρ_m is the non-relativistic matter (including dark matter and baryons) density of the Universe. The structure formation in the non-linear regime is well studied by assuming the quasi-static and weak-field approximations (Bose, Hellwing & Li 2015). Under such limits equation (2) reduces to the Poisson equation

$$\nabla^2 \Phi = 4\pi G a^2 \delta \rho_m - \frac{1}{2} \nabla^2 f_R, \quad (4)$$

and equation (3) is

$$\nabla^2 f_R = \frac{a^2}{3} (\delta R(f_R) - 8\pi G \delta \rho_m), \quad (5)$$

where Φ represents the gravitational potential at some particular position in the space and corresponding to the density fluctuation $\delta \rho_m = \rho_m - \bar{\rho}_m$ with curvature perturbation $\delta R = R - \bar{R}$. Here $\bar{\rho}_m$ and \bar{R} are the background matter density and the curvature of the Universe, respectively. This system of equations determines the effect of MG on the structure formation. While in case of Λ CDM model, the Poisson equation has form $\nabla^2 \Phi = 4\pi G a^2 \delta \rho_m$. Therefore, the term $\nabla^2 f_R$ in equation (4) drives the MG effect in comparison to Λ CDM model.

Different forms of $f(R)$ gravity models have been proposed in the literature (see e.g. Capozziello & Fang 2002; Chiba 2003; Dolgov & Kawasaki 2003; Nojiri & Odintsov 2003; Faraoni 2006; Hu & Sawicki 2007; Cognola et al. 2008; Linder 2009).

For this work, we consider the most widely studied functional form of $f(R)$, proposed by Hu & Sawicki (2007) which satisfies both cosmological and Solar system tests (Martinelli, Melchiorri & Amendola 2009)

$$f(R) = -m^2 \frac{c_1 \left(-\frac{R}{m^2}\right)^n}{c_2 \left(-\frac{R}{m^2}\right)^n + 1}. \quad (6)$$

Here n , c_1 , and c_2 are dimensionless model parameters and $m^2 = H_0^2 \Omega_{m0}$ with H_0 and Ω_{m0} are respectively the present day values of the Hubble constant and the matter density parameters of the Universe. If we set $c_1/c_2 = \Omega_{\Lambda0}/\Omega_{m0}$, with $\Omega_{\Lambda0} \equiv 1 - \Omega_{m0}$, the model is able to mimic the expansion history of Λ CDM. From equation (6) the functional form of the scalaron field, f_R , is given by

$$f_R = -\frac{c_1}{c_2} \frac{n(-R/m^2)^{n-1}}{[(-R/m^2)^n + 1]^2}, \quad (7)$$

where

$$\frac{c_1}{c_2} = -\frac{1}{n} \left[3 \left(1 + 4 \frac{\Omega_{\Lambda0}}{\Omega_{m0}} \right) \right]^{(n+1)} f_{R0}, \quad (8)$$

with f_{R0} is the present value of the scalaron field.

We notice that from equation (8), n and f_{R0} are the remaining free parameters of the model. Hence, in this work we adopt the values $n = 1$ and $|f_{R0}| = 10^{-6}$, 10^{-5} , and 10^{-4} (hereafter referred as F6, F5, and F4, respectively) which correspond to a weak, medium, and strong deviation with respect to GR, i.e. to Λ CDM model.

The aim of this work is to study the effect of MG models under different density environments. Thus, it is important to understand the screening mechanism implemented in such models that could have a direct impact in the halo (and thus galaxy) density field. Recall that the screening mechanisms are applied in MG models to suppress the enhancement of the fifth force in order to pass high precision tests of gravity in the high-dense regions like the Solar system (see e.g. Vainshtein 1972; Khoury & Weltman 2004). To suppress the effects of the fifth force in high-density regions, the Hu–Sawicki $f(R)$ gravity model employs the chameleon mechanism (Khoury & Weltman 2004), where the scalaron field which mediates the fifth force has a non-zero mass, $m_{f_R}^2 = \partial^2 V_{\text{eff}} / \partial^2 f_R$, depending on the non-linear terms in the equation of motion, see equation (3). The corresponding fifth force is of Yukawa-type, decaying exponentially with mass as $\propto \exp(-m_{f_R} r)$ where r is the separation between two test masses. Under the high-density environments, this scalaron field is massive and because of it, the fifth force is suppressed

sufficiently and allows to recover GR successfully. Depending on the requirement of screening different density environments of our Universe, various constraints on the f_{R0} values are being studied in the literature (for recent reviews see Jain, Vikram & Sakstein 2013; Vikram et al. 2013; Lombriser 2014; Burrage & Sakstein 2016).

Recent studies based on Milky-Way-type galaxies, being need to be screened in order to satisfy the Solar system test, imposes the constraint on the present day value for the scalaron field to be within the range of $|f_{R0}| < 10^{-4}$ – 10^{-6} (Hu & Sawicki 2007), while for dwarf galaxies, it has been reported the values as low as $|f_{R0}| \lesssim 10^{-7}$ (Lombriser 2014). On the other hand, the abundance of galaxy clusters, based on X-ray data, in combination with the CMBR, based on the Planck measurement, and SNIa and BAOs, Cataneo et al. (2015) found an upper value of $|f_{R0}| < 1.6 \times 10^{-5}$ at the 95.4 per cent confidence level.

2.2 nDGP model

In the Dvali–Gabadadze–Porrati (DGP) braneworld cosmological model (Dvali et al. 2000), the standard four-dimensional spacetime universe (or brane) is embedded in a five-dimensional bulk space–time with an infinite extra dimension; the standard matter particles are confined only on the brane surface. In this model, the graviton field is freely propagated into the extra dimension (Koyama & Silva 2007). Thus, the modifications of Einstein’s general relativity are quantified in the action:

$$S = \int_{\text{brane}} d^4x \sqrt{-g} \frac{R}{2\kappa} + \int_{\text{bulk}} d^5x \sqrt{-g^{(5)}} \frac{R^{(5)}}{2\kappa^{(5)}} + S_m(g_{\mu\nu}, \psi_m) \quad (9)$$

where $\kappa^{(5)} = 8\pi G^{(5)}$ with $G^{(5)}$ being the 5D gravitational constant and $R^{(5)}$ is the Ricci scalar in five dimensions. The gravitational constants in the brane (G) and in the bulk ($G^{(5)}$) are related through the cross-over scale, r_c ,

$$r_c = \frac{1}{2} \frac{G^{(5)}}{G}, \quad (10)$$

where below this scale the strength of four-dimensional gravity becomes dominant and vice versa.

Here, we consider the *normal branch* of the DGP model, nDGP, where a dark energy component is included to the matter part of action in order to have an accelerated expansion of the Universe (Schmidt 2009). Hence the expansion rate under such scenario is given by

$$H(a) = H_0 \left(\sqrt{\Omega_m a^{-3} + \Omega_{DE}(a) + \Omega_{rc}} - \sqrt{\Omega_{rc}} \right), \quad (11)$$

with Ω_{DE} is the contribution of the dark energy component and $\Omega_{rc} = 1/(4H_0^2 r_c^2)$ is a dimensionless parameter related to the cross-over scale. From equation (11) we notice that in the limit $\Omega_{rc} \rightarrow 0$ or $H_0 r_c \rightarrow \infty$ we recover the expansion history of the Λ CDM model. Here, we consider two variants of the nDGP model with $H_0 r_c = 5$, N5, and $H_0 r_c = 1$, N1, which represent models with a weak and medium deviation with respect to GR, respectively.

Similar to $f(R)$ gravity models, the appearance of a new scalar field, φ , associated with the bending modes of the 4D brane mediates the fifth force. In this model, the modified Poisson equation and the equation of motion for the scalar field φ under the quasi-static approximation are given by (Koyama & Silva 2007)

$$\nabla^2 \Phi = 4\pi G a^2 \delta\rho_m + \frac{1}{2} \nabla^2 \varphi, \quad (12)$$

with

$$\nabla^2 \varphi + \frac{r_c^2}{3\beta a^2} [(\nabla^2 \varphi)^2 - (\nabla_i \nabla_j \varphi)^2] = \frac{8\pi G a^2}{3\beta} \delta\rho_m, \quad (13)$$

and

$$\beta = 1 + 2H r_c \left(1 + \frac{\dot{H}}{3H^2} \right). \quad (14)$$

Here, the term $\nabla^2 \varphi$ in the Poisson equation (12) governs the MG effect. One can understand the screening mechanism employed in this model by simply considering the spherically symmetric geometry in which the field equation, equation (13), has an analytic solution given by (Koyama & Silva 2007):

$$\varphi_{,r} = \frac{4}{3\beta} \left(\frac{r}{r_V} \right)^3 \left[-1 + \sqrt{1 + \left(\frac{r_V}{r} \right)^3} \right] \frac{GM(r)}{r^2}. \quad (15)$$

Here r_V is a distance scale called Vainshtein radius defined as

$$r_V(r) = \left(\frac{16r_c^2 GM(r)}{9\beta^2} \right)^{1/3}, \quad (16)$$

where $M(r) = 4\pi \int_0^r dr' r'^2 \delta\rho_m(r')$ is the mass enclosed within a radius r . This Vainshtein radius is an important quantity that provides the limit on the distance from the centre of overdensity of $M(r)$ below which the fifth force is suppressed efficiently; the so called the Vainshtein screening mechanism (Vainshtein 1972).

In other words, if we consider the ratio of fifth force, F_{5th} to Newtonian forces, F_N :

$$\frac{F_{5th}}{F_N} = \frac{\varphi_{,r}}{\Phi_{N,r}} \rightarrow 0, \quad \text{as} \quad \frac{r}{r_V} \rightarrow 0, \quad (17)$$

the fifth force is suppressed near massive objects where $r < r_V$ and $\varphi_{,r} \rightarrow 0$, allowing the model to recover GR in high-density regions.

The nature of Vainshtein mechanism makes difficult to test such models in small scales in the non-linear regime. But constraints from the Solar system set an upper value of $[r_c H_0]^{-1} < 0.1$ (Koyama 2016). On the other hand, observations of luminous red galaxies from the BOSS-DR12 sample constrains the parameter to $[r_c H_0]^{-1} < 0.97$ (Barreira, Sánchez & Schmidt 2016).

3 N-BODY SIMULATIONS

This Section describes the N -body simulations employed for this work. Here, we use six different N -body simulations corresponding to different gravity models, including the standard Λ CDM one, based on GR. In this paper, we consider two different sets of MG models (as we explained above): the chameleon $f(R)$ gravity and the normal branch of the DGP braneworld model.

All the simulations were generated using the adaptive-mesh-refinement AMR code ECOSMOG (Li et al. 2012, 2013) based on the WMAP9 background cosmology (Hinshaw et al. 2013): $\Omega_{m0} = 0.281$, $h = 0.697$, and $n_s = 0.971$. The simulation are in boxes of side length of $1024 h^{-1}$ Mpc, with 1024^3 dark matter particles, and the respective particle mass of $m_p = 7.8 \times 10^{10} h^{-1} M_\odot$, with a power spectrum normalization of $\sigma_8 = 0.82$. Initial conditions for all the simulations were generated using the Zel’dovich approximation with the publicly available MPGRAFIC code (Prunet et al. 2008) at $z_{ini} = 49$. We use the outputs at $z = 0$.

The $f(R)$ and nDGP model parameters were chosen such that they deviate from Λ CDM only at later times. At z_{ini} MG effects can be neglected, and thus all simulations were run with the

Table 1. The cosmological parameters and specifications of the N -body simulations.

Parameter	Definition	Value
Ω_m	Present matter density	0.281
Ω_Λ	$1 - \Omega_m$	0.719
h	$H_0/(100 \text{ km s}^{-1} \text{ Mpc}^{-1})$	0.697
n_s	Primordial power spectral index	0.971
σ_8	r.m.s. linear density fluctuation	0.820
$ f_{R0} $	Hu & Sawicki $f(R)$ parameter	10^{-6} (F6), 10^{-5} (F5), 10^{-4} (F4)
$H_0 r_c$	nDGP parameter	5 (N5), 1 (N1)
L_{box}	Simulation box size	$1024 h^{-1} \text{ Mpc}$
N_p	Simulation particle number	1024^3
m_p	Simulation particle mass	$7.78 \times 10^{10} h^{-1} M_\odot$
N_{dc}	Domain grid cell number	1024^3

same initial condition. The maximal force resolution in all the simulations from the adaptive-mesh-refinement (AMR) technique is of $0.015 h^{-1} \text{ Mpc}$. This allows us to resolve overdense regions where the screening effect is strong.

For more details about the simulations, we refer the reader to Li et al. (2012) and Bose et al. (2017) for the $f(R)$ case, and Li et al. (2013) and Barreira, Bose & Li (2015) for the nDGP case. The cosmological and technical parameters are given in Table 1. At $z = 0$, each simulation has five realizations which were run by slightly different initial conditions in the random phases of the density field. Except for F4 model where there are only two realizations available. We use these realizations to understand the statistical uncertainties in our results.

Halo and subhaloes were identified with the phase-space temporal halo finder ROCKSTAR⁵ (Behroozi, Wechsler & Wu 2013a). Here, we use the halo mass definition of $M_{200c} \equiv \frac{4\pi}{3} 200\rho_c R_{200c}^3$ which corresponds to haloes enclosing 200 times the critical density of the Universe, ρ_c within the radius R_{200c} . In all the six halo catalogues, we provide a limit in the number of particles contained in the haloes, i.e. at least the halo must contain 50 or more particles. This leads to the resolution limit in the maximum circular velocity of dark matter haloes, $V_{\text{max}} \sim 257 \text{ km s}^{-1}$.

3.1 Dark matter halo demographics

Fig. 1 shows the differential maximum circular velocity functions, $\phi_V(V_{\text{max}})$, for distinct dark matter haloes (left-hand panel) and subhaloes (right-hand panel) for all the gravity models at redshift $z = 0$. Here, subhaloes are those haloes, whose radius is inside of a larger halo; distinct haloes cannot be subhaloes by definition. The black solid, blue dotted, green dash-dotted, red dashed, magenta medium dashed, and orange long dashed lines represent GR, F6, F5, F4, N5, and N1 models, respectively. We will use this convention for all the figures representing these models throughout the paper. The lower panel shows the relative difference w.r.t. the Λ CDM (GR) simulation, and the corresponding shaded areas represent the error propagated from the 1σ standard deviation measurement of all the realizations available as described above. The differential maximum circular velocity function, $\phi_V(V_{\text{max}})$, shown in both panels are the mean of all the realizations for each gravity model analysed in this paper.

We begin by describing the differences with the distinct halo velocity functions. As expected from theoretical arguments, see

Section 2, we observe that in general, the smaller the value of the f_{R0} parameter, the closer $\phi_V(V_{\text{max}})$ to the standard Λ CDM model.

Based on the above, it is reasonable that the F4 model presents a significant difference from the standard Λ CDM model. This is also true when analysing the nDGP models, especially at the high-velocity end both for distinct haloes and subhaloes.

Fig. 1 has various points that are worth to highlight. We focus first on $f(R)$ gravity models and divide our discussion into three different velocity ranges: (1) $V_{\text{max}} < 500 \text{ km s}^{-1}$; (2) $500 \text{ km s}^{-1} \leq V_{\text{max}} < 1000 \text{ km s}^{-1}$; and (3) $1000 \text{ km s}^{-1} \geq V_{\text{max}}$. The reason for the above three velocity ranges is that the behaviour of the velocity functions for the $f(R)$ gravity models vary with the present day value of f_{R0} as can be seen in the bottom panel of Fig. 1. This panel shows that F6 has a maximum excess of abundance of haloes of ~ 25 per cent w.r.t. the Λ CDM for haloes with $V_{\text{max}} < 500 \text{ km s}^{-1}$ whereas both F5 and F4 remain roughly similar to the Λ CDM model. The recent analysis of high-resolution N -body simulations in Shi et al. (2015) shows that the halo mass function of F6 has an excess ~ 20 per cent w.r.t. the Λ CDM for haloes below $M_{200} \sim 10^{13} h^{-1} M_\odot$, which is equivalent to our velocity range and thus consistent with our results. The authors interpreted the above as the result of the chameleon screen mechanism begins less efficient in those dark matter haloes, see also fig. 8 in Falck et al. (2015). Additionally, the authors showed that the halo profiles for those haloes are significantly steeper in their inner regions than their GR counterparts. In consequence, their halo concentrations are enhanced and therefore their V_{max} . This further explains why we observe the above difference between F6 and the Λ CDM model at these velocities.

For haloes with $500 \text{ km s}^{-1} \leq V_{\text{max}} < 1000 \text{ km s}^{-1}$, we find an abrupt deviation for F5 w.r.t. Λ CDM of 50 per cent. The difference peaks at $V_{\text{max}} \sim 630 \text{ km s}^{-1}$ but it decreases for both low and high velocities. In the case of F4 there is a clear systematic increase in the abundance of haloes, reaching an excess of ~ 50 per cent at $V_{\text{max}} \sim 1000 \text{ km s}^{-1}$ while F6 remains very similar to the Λ CDM model. The above differences observed in F5 are also a direct consequence of the chameleon screen mechanism. As shown in Li & Efstathiou (2012), a feature of the chameleon screen mechanism is to produce an excess of dark matter haloes within some mass range. This leads to a compensation effect by decreasing the number of low-mass haloes⁶ due to the hierarchical mass assembling process of dark matter haloes. On the other hand, as these authors noted, in high-mass haloes the chameleon screen mechanism is very efficient in addition that the fifth force is suppressed due to high-mass haloes living in

⁵<https://bitbucket.org/gfstanford/rockstar>

⁶We do not observe this decrease due to resolution limits in the suite of simulations we are using.

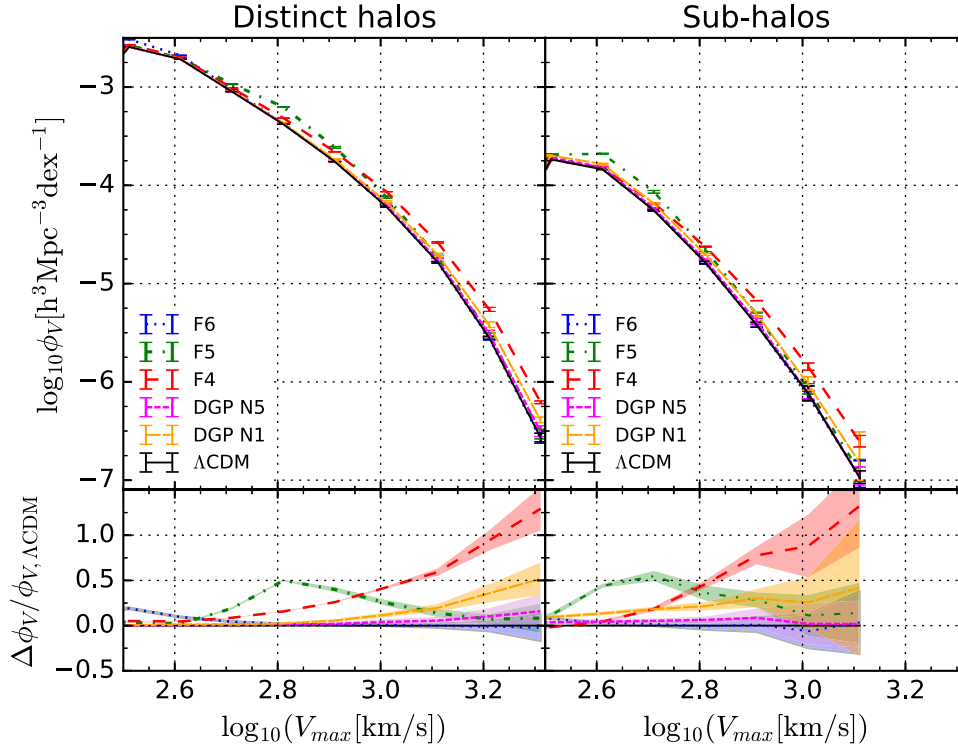


Figure 1. Differential V_{\max} function of the distinct and subhaloes for the MG models considered here along with the Λ CDM model. The black solid, blue dotted, green dot–dashed, red dashed, magenta medium-dashed, and orange long-dashed lines represent Λ CDM(GR), F6, F5, F4, N5, and N1, respectively. This convention will be followed in the rest of the plots. The relative differences w.r.t. the Λ CDM are shown in the lower panel, where the shaded regions show the error propagated from the 1σ standard deviations of all the realizations available. On comparing this figure with the corresponding halo mass functions and mass–concentration relations showed in Fig. A1, a similar behaviour is observed.

dense environments; thus, the abundance of high-mass dark matter haloes approaches to the Λ CDM model. Indeed, we observe that this is the case for the F5 model. In Appendix A we present the corresponding halo mass functions in the left-hand panel of Fig. A1. Here the excess in the F5 model is evident and consistent with the discussion from Li & Efstathiou (2012). Additionally, we also observe that halo concentrations in the F5 model are significantly enhanced within the mass range of halo excess (right-hand panel of Fig. A1), consistent when extrapolating the result from Shi et al. (2015).

In general, the mass range at which the chameleon screen mechanisms produce an excess of dark matter haloes depends on the present day value of the scalaron field f_{R0} , see fig. 9 from Li & Efstathiou (2012). The higher the value in f_{R0} , the larger the halo masses where the excess of dark matter haloes happens and the larger this excess. Finally, the increase of dark matter haloes for F4 at $V_{\max} \gtrsim 1000 \text{ km s}^{-1}$ is just a consequence of the above. We thus conclude that the trends we observe over the full velocity range is result of the chameleon screen mechanism and its effects depending on the present day value of the scalaron field f_{R0} . Similar results have been noted in previous works using N -body simulations (see e.g. Li et al. 2012, 2013; Hernández-Aguayo, Baugh & Li 2018).

As for the nDGP models, we observe marginal deviations from the Λ CDM. These deviations are in the expected direction as we observe that N1 has an excess of haloes at $V_{\max} \gtrsim 1000 \text{ km s}^{-1}$ but N5 remains very similar to the Λ CDM model. Finally, in the case of the subhaloes, we observe a similar behaviour to distinct haloes but with larger uncertainties, which makes difficult to conclude over the significance of the result. None the less, similar results have been reported in Shi et al. (2015) for the F6 model.

The above differences show the effect of the different screening mechanisms over all ranges of V_{\max} . Due to the extreme nature of gravity in F4 and N1 models, the corresponding screening mechanism (chameleon or Vainshtein) is less efficient for massive haloes, i.e. haloes with larger $V_{\max} \gtrsim 1000 \text{ km s}^{-1}$, leading to an increase in the number density of haloes in these models. For F5, the inefficiency of the chameleon screening mechanism appears in haloes with intermediate values of $V_{\max} \sim 600 \text{ km s}^{-1}$, as discussed above. On the other hand, the difference is small for F6 and N5 models w.r.t. Λ CDM.

4 THE GALAXY–HALO CONNECTION IN MODIFIED GRAVITY SIMULATIONS

To assign galaxies to the dark matter haloes we use the SHAM. The match is between the SDSS r -band luminosity function and the V_{\max} halo function, and then we obtain the M_r – V_{\max} relation. In this section, we show that the M_r – V_{\max} relation, for both central and satellite galaxies, varies among the models with differences below ~ 1 per cent, which corresponds to differences of ~ 0.2 mag at a fixed V_{\max} . We also show that the different models predict similar galaxy clustering, which are in good agreement with observations.

4.1 Subhalo abundance matching: SHAM

Subhalo abundance matching, SHAM, is a simple rule that connects dark matter halo properties to galaxy properties under the assumption that there is a one-to-one monotonic relation between galaxies

and dark matter halo properties. In addition, SHAM assumes that centrals and satellite galaxies have identical relationships. In this work we decide to use the maximum circular velocity of dark matter haloes V_{\max} as our halo property and r -band magnitudes for galaxy properties.

The standard assumptions in SHAM have been criticized in previous studies (see e.g. Rodríguez-Puebla, Drory & Avila-Reese 2012; Yang et al. 2012; Rodríguez-Puebla, Avila-Reese & Drory 2013). These studies have shown that assuming similar relations for centrals and satellites could lead to potential inconsistencies, particularly in reproducing galaxy clustering and the observed counts from conditional stellar mass functions (for a more detail discussion see Rodríguez-Puebla et al. 2012). Following Rodríguez-Puebla et al. (2012), we choose to separately derive relations for centrals and satellites as we will explain in more detail below.

As mentioned above, in order to perform SHAM we consider to use the maximum circular velocity of haloes, V_{\max} , as the main halo property that correlates with galaxy luminosities. Indeed, previous studies (e.g. Conroy et al. 2006; Reddick et al. 2013; Campbell et al. 2018) have shown that when using V_{\max} for dark matter haloes, the galaxy clustering is in much better agreement with observations. In particular, the above works have shown that using halo V_{\max} at $z \sim 0$ for distinct haloes and the highest V_{\max} reached along the main progenitor branch of the halo's merger tree, typically referred as V_{peak} , for subhaloes, give much better results. This is because the properties of a halo's central region, where central galaxies reside, are better described by V_{\max} than halo mass. Unfortunately, values for V_{peak} are not available in our set of simulations and contrary to other works, here we use V_{\max} for both distinct and subhaloes. Note however, that Rodríguez-Puebla et al. (2012) showed that using separate relationships for central and satellites, the spatial galaxy clustering is well recovered even when employing only current ($z \sim 0$) halo properties. Using a similar approach as in that paper, we will show that our mock galaxy catalogues are able to recover the observed spatial galaxy clustering. Finally, we mention that SHAM has been applied for $f(R)$ models in previous works (see e.g. He, Li & Baugh 2016).

Next, we discuss the observational inputs that we use for the SHAM, that is, the SDSS r -band luminosity functions of central and satellite galaxies.

4.1.1 r -band luminosity functions

Here, we use the SDSS DR7 r -band luminosity function measured in Dragomir et al. (2018) for all galaxies. The authors used the New York Value Added Galaxy Catalog (NYU-VAGC; Blanton et al. 2005) based on the SDSS DR7 which comprises a catalogue of $6 \sim 10^5$ spectroscopic galaxies over a solid angle of 7748 deg^2 in the redshift range $0.01 < z < 0.2$. The authors K + E-corrected r -band absolute magnitudes at $z = 0$. In order to derive the luminosity function for centrals and satellites we used the results from Yang, Mo & van den Bosch (2009). Using the NYU-VAGC based on the SDSS DR4, Yang et al. (2009) derive the r -band luminosity functions for centrals and satellites separately. Below, we describe our best-fitting model to the fraction of satellite galaxies as a function of r -band luminosity.

The fraction of satellite galaxies is defined as the ratio of the satellite luminosity function to the total, $f_{\text{sat}} = \phi_{\text{sat}}/\phi_{\text{tot}}$; the fraction of central galaxies is simply $f_{\text{cen}} = 1 - f_{\text{sat}}$. After some experimentation with different functional forms, we find that the

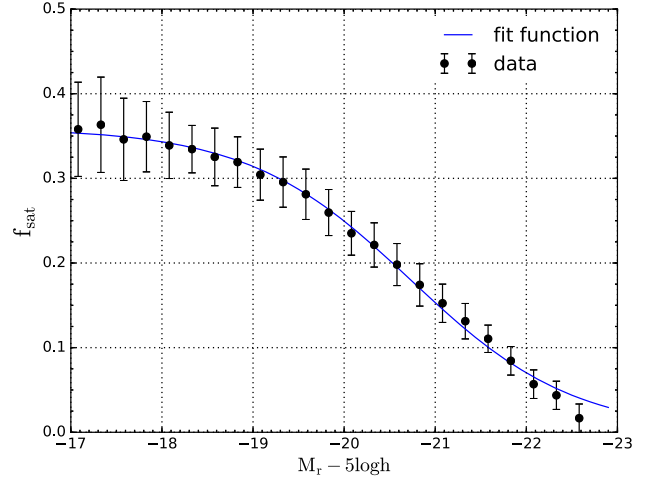


Figure 2. Satellite fraction as a function of $M_r - 5 \log h$. The black dot with error bars corresponds to the fraction of satellites inferred by Yang et al. (2009) from the SDSS data, and the blue line is the best fit using the function equation (18).

following function reproduces accurately the observations:

$$f_{\text{sat}}(M_r) = \frac{A}{(1 + 10^{\alpha(M^* - M_r)})}, \quad (18)$$

where A is an amplitude, M^* is the characteristic magnitude at which the fraction $f_{\text{sat}} = A/2$, and α controls the slope of the fraction at the massive-end. Note that in equation (18) we use r -band absolute magnitudes M_r while Yang et al. (2009) reported luminosities. We use $\log L = -0.4 \times (M_r - M_{r,\odot})$ with $M_{r,\odot} = 4.67$. Fig. 2 shows the observed fraction of satellite galaxies as a function of M_r magnitude, filled circles with error bars. We find that the best fitting values are $(A, M^*, \alpha) = (0.357, -20.741, 0.504)$, the best-fitting model is shown as the blue solid line.

We use the above best-fitting model to derive the r -band luminosity function separately for centrals and satellites for SHAM. As mentioned above, we are considering the luminosity function from Dragomir et al. (2018). Specifically, we use their best-fitting model to a modified double Schechter function, see their equation 4, with their best-fitting parameters reported in their table 1.

4.1.2 Results on the galaxy–halo connection

We apply SHAM separately for centrals and satellites to find the $M_r - V_{\max}$ relation (Rodríguez-Puebla et al. 2012). For centrals we use

$$\int_{M_r}^{\infty} \phi_{\text{cen}}(M'_r) dM'_r = \int_{V_{\max}}^{\infty} \phi_{V,\text{haloes}}(V'_{\max}) d \log V'_{\max}, \quad (19)$$

and similarly for satellites

$$\int_{M_r}^{\infty} \phi_{\text{sat}}(M'_r) dM'_r = \int_{V_{\max}}^{\infty} \phi_{V,\text{subhaloes}}(V'_{\max}) d \log V'_{\max}. \quad (20)$$

Note that the above form of SHAM implies zero-scatter in the $M_r - V_{\max}$ relations.

Fig. 3 shows respectively the resulting $M_r - V_{\max}$ of centrals and satellites in the left and right upper panels for the models considered, respectively. We also compared to the results from Dragomir et al. (2018), who applied the same SHAM we use here. Dragomir et al. (2018) derived the above relation for all type

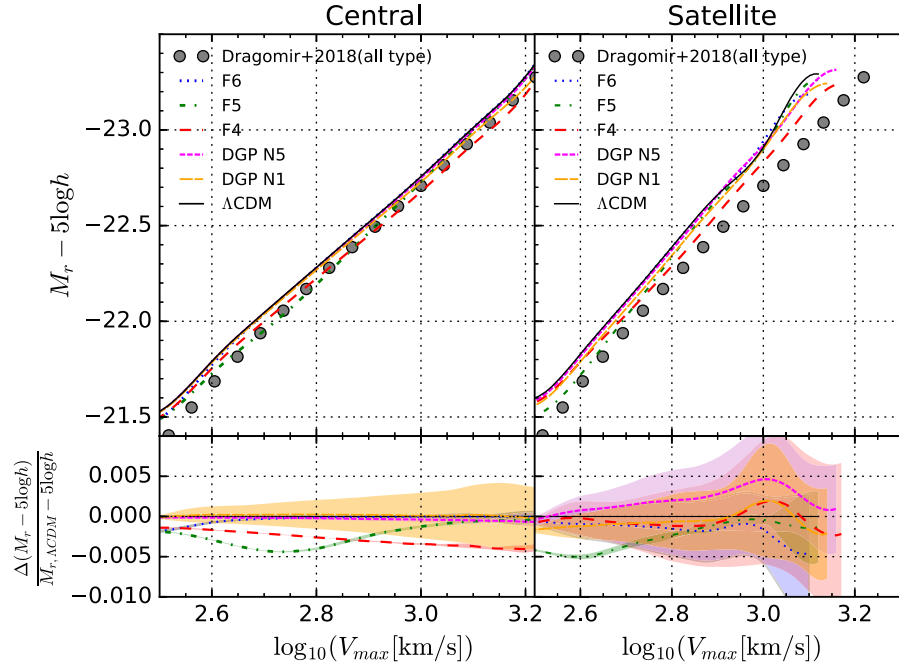


Figure 3. Obtained central and satellite M_r – V_{\max} relations by means of the SHAM method for our different gravity models. The relative differences w.r.t. Λ CDM are shown in the lower panel. The result of Dragomir et al. (2018) for all type galaxies (see appendix A of their paper) is reproduced in both panels with grey filled circles. Some differences in M_r – V_{\max} relation are observed in all MG models with respect to Λ CDM but the variations are < 1 per cent, mostly within the 0.5 per cent.

galaxies; as discussed in Rodríguez-Puebla et al. (2012) the relation for all galaxies is closer to the one of centrals than for satellites. Differences with Dragomir et al. (2018) is just mainly the result of different cosmological parameters: these authors used a cosmology based on the results from Planck 2016 (Planck Collaboration XIII 2016), while here we use a cosmology that is closer to the results from the WMAP9 mission.⁷ One can see in figs 10 and 15 of Rodríguez-Puebla et al. (2016a) the ratio of the predicted distinct halo number densities between the Bolshoi-Planck and Bolshoi-WMAP7 ($\Omega_m = 0.27$, similar to WMAP9) simulations; similar differences are observed by us. Due to this difference, a slightly higher number density of dark matter haloes at a fixed halo mass/ V_{\max} are found in the Bolshoi-Planck simulation than in our simulation. The SHAM translates this into a shift to higher values of V_{\max} for a given luminosity. Note also that the SHAM in Dragomir et al. (2018) was applied to all haloes while here we separate into distinct haloes and subhaloes.

The lower panels in Fig. 3 present the differences in the M_r magnitudes at a fixed V_{\max} for all the MG models with respect to the standard Λ CDM model. The shaded regions show the 1σ standard deviation calculated using five realizations except for F4, for which we consider only two realizations. Observe that these differences are just a direct result of the differences between the velocity functions described in the previous subsection (see Fig. 1), and not to different cosmological parameters since all of our simulations use the same cosmological parameters. Fig. 3 shows that the differences in M_r for the MG models with respect to the Λ CDM (GR) one is not larger than 1 per cent. This statement is valid for both central and satellite galaxies.

Indeed, in both cases the differences in M_r for all the models is within 0.5 per cent. The above is especially true for F4 and F5 MG models. Note that N1 and N5 models are closer to the Λ CDM for the particular case of central galaxies. Note that these differences are not related to uncertainties in the determination of the M_r – V_{\max} relationship but true deviations due to the different gravity models. As noted above they resemble the differences in the velocity functions. In terms of magnitudes the differences are up to ~ 0.2 mag. We do not propagate uncertainties due to observations as it will be the same for all the models. Next, we discuss errors in the M_r – V_{\max} relationship determinations.

We measure uncertainties around the M_r – V_{\max} relationships by using the various realizations from our suite of simulations, shown as shaded areas in the lower panels of Fig. 3. This figure shows that for central galaxies N1 has the largest error when determining the M_r – V_{\max} relationship over all realizations. However, it is not larger than ~ 0.5 per cent, see orange shaded area. In the case of satellite galaxies, their number is much lower than centrals and thus more dominated by Poissonian error. While we expect larger uncertainties for satellites, we observe uncertainties not larger than ~ 1 per cent in most of the models. The fact that uncertainties, both for central and satellites, are smaller than ~ 1 per cent in the M_r – V_{\max} relationship guarantees accurate mock galaxy catalogues, and that cosmic variance is not an extra uncertainty in our determinations. In other words, *differences in our resulting predictions based on the mock catalogues will be the result of the differences among the different gravity models rather than in the technique itself or from cosmic variance.* We will come back to this in Section 6.

4.2 Spatial galaxy clustering

As a standard procedure, we show that our resulting M_r – V_{\max} relations for centrals and satellites is consistent with the observed

⁷For Planck 2016, the total matter density at the present day is $\Omega_m \approx 0.308$ whereas for WMAP9, this density is lower, $\Omega_m \approx 0.28$.

projected two-point correlation functions from the SDSS DR7 (Zehavi et al. 2011). Indeed, spatial galaxy clustering should be considered as a consistency test for the mock galaxy catalogues that we generated for all the MG models.

Zehavi et al. (2011) derived the projected two-point correlation function in the r -band magnitude at $z = 0.1$ for several magnitude thresholds. Recall that in this paper we are using the results from Dragomir et al. (2018), who used r -band magnitude at $z = 0$. In order to make a fair comparison between our predicted and the projected two-point correlation from Zehavi et al. (2011), we transform our r -band magnitudes to $z = 0.1$ using the relationship reported in Dragomir et al. (2018).

Fig. 4 shows the projected two-point correlation function for two magnitude thresholds; $M_r - 5\log h < -21.5$ and $M_r - 5\log h < -22$ in left-hand and right-hand panels, respectively. The middle and bottom panels show the relative differences of the different gravity models with respect to observations from the SDSS DR7, and of the MG models with respect to the Λ CDM (GR) model, respectively. The black error bars (showed only for the Λ CDM model) correspond to the uncertainties propagated from the observations, and the shaded areas show the 1σ error estimated using the realizations available for each gravity model.

There are various points to highlight from this figure. First, note that SHAM reproduces the projected two-point correlation functions for $M_r - 5\log h < -21.5$ ($M_r - 5\log h < -22$) within the ~ 20 per cent (~ 30 per cent) for all gravity models, see the middle panels of Fig. 4. As mentioned above the shaded areas show the dispersion from all the realizations of the simulations employed in this paper. Within the uncertainties, all the simulations are recovering acceptable correlation functions. Note, however, that there are systematic trends as a function of the projected radius that are independent of the gravity models employed in this paper. This implies that the differences from observations as a function of radius are not particularly intrinsic to some type of gravity model but a systematic arises when assigning galaxies to haloes. Is this a sign that SHAM fails in reproducing galaxy clustering even in the case of the standard Λ CDM? There are several understandable reasons why our models do not reproduce to a much higher accuracy galaxy clustering. The most obvious one is that we have assumed no scatter in the $M_r - V_{\max}$ relation both for centrals and satellites. The impact of including scatter reduces galaxy clustering at large projected distances as shown in Reddick et al. (2013). Even a moderate value of scatter, ~ 0.2 dex, reduces galaxy clustering for large distances but does not affect significantly the clustering at small distances, see fig. 5 from Reddick et al. (2013). This will simply explain why our galaxy mock models tend to overestimate more the two halo-term (larger distances) than the one halo term in both panels. Since all the gravity models follow the same trend in the difference with the observed galaxy clustering, we do not consider this difference as an extra source of uncertainty for our further comparative study among the different gravity models.

In more detail, we observe that the degree of agreement with respect to the observation as a function of the scale may be slightly different for each gravity model. For the magnitude limit of $M_r - 5\log h < -21.5$, the Λ CDM model, on average, remains within ~ 10 per cent below $r_p \sim 2 \text{ Mpc } h^{-1}$ and, on average, it deviates around ~ 20 per cent above $r_p \sim 10 \text{ Mpc } h^{-1}$. Surprisingly, F4 is on average closer to the observations, within ~ 10 per cent at all scales; recall that for this model, its velocity function significantly deviates from the Λ CDM one. For the magnitude limit of $M_r - 5\log h < -22$, note that uncertainties become larger both in observations as well as in the theoretical prediction of projected correlation functions. The

reason behind it is quite simple as the number of brighter galaxies decreases both in the SDSS DR7 survey and in our mock galaxy catalogues. We expect that with on-going and future surveys, as well as with larger N -body simulations, the measurements of the galaxy clustering will improve further and will be sensitive enough to discriminate among different MG models. Here, despite of the differences described above it becomes difficult to conclude which MG model describes better the current observed galaxy clustering. Additionally, recall that our SHAM does not include scatter around the $M_r - V_{\max}$ relation. Even more, this scatter could be different for the different gravity models. In any case, the aim of this work is not to use galaxy clustering as a discriminant of gravity models. We just wanted to show that the SHAM applied to each one of the gravity models predicts spatial galaxy clustering in rough agreement with observations, and that differences in the clustering of the MG models with respect to the Λ CDM are mostly within the 10 per cent.

4.3 Halo occupation distribution model: HOD

In the context of SHAM, the halo occupation distribution of galaxies in dark matter haloes arises naturally. In this section, we explore and quantify the resulting halo occupation distribution (HOD) based on SHAM for our set of different gravity models. So far, HOD remains as one of the most powerful tools to connect the galaxies to the cold dark matter haloes, with the aim to constraint various physical processes that govern the galaxies formation and its evolution (for a review see, Wechsler & Tinker 2018). None the less, HOD is not only a powerful tool for constraining galaxy formation but it is also a useful tool to constrain cosmology (see e.g. Yang, Mo & van den Bosch 2003; van den Bosch et al. 2013; More et al. 2013, 2014, and references therein). Thus, it is interesting to study the changes in HOD under different cosmological scenarios specially when applying SHAM results in different $M_r - V_{\max}$ relations.

Briefly, the HOD quantifies the probability of finding N galaxies above some magnitude threshold within a given halo with mass M_{200c} . Here, we calculate the mean occupation of central and satellite galaxies above the limit of $M_r - 5\log h < -21.5$. Fig. 5 shows the resulting HOD separately for centrals and satellites. Next we describe the best fitting functions to our HOD models and provide separate fits to the satellite and central mean occupation functions for all the gravity models studied in this paper. For the mean occupation of satellites, we use the standard power law with an exponential decreasing function that consists of three free parameters (Kravtsov et al. 2004):

$$\langle N_{\text{sat}}(M_{200c}) \rangle = \left(\frac{M_{200c}}{M_1} \right)^\alpha \exp \left(-\frac{M_{\text{cut}}}{M_{200c}} \right), \quad (21)$$

where the parameter M_1 corresponds to the mass scale at which haloes host at least a satellite on average, M_{cut} , the mass scale below which the satellite mean occupation starts to decay exponentially and α provides the power-law slope of the relation between halo mass M_{200c} and N_{sat} . On the other hand, for the mean occupation function of central galaxies, we consider the standard error function representation:

$$\langle N_{\text{cen}}(M_{200c}) \rangle = \frac{1}{2} \left(1 + \text{erf} \left(\frac{\log M_{200c} - \log M_{\min}}{\sigma_{\log M}} \right) \right), \quad (22)$$

where erf is an error function $\text{erf}(x) = \frac{2}{\sqrt{\pi}} \int_0^x \exp(-t^2) dt$. The M_{\min} is the minimum mass at which a halo hosts at least one central galaxy and $\sigma_{\log M}$ width of the transition between $N_{\text{cen}} = 0$ and $N_{\text{cen}} = 1$. Under the assumption that the HODs of central and satellite galaxies

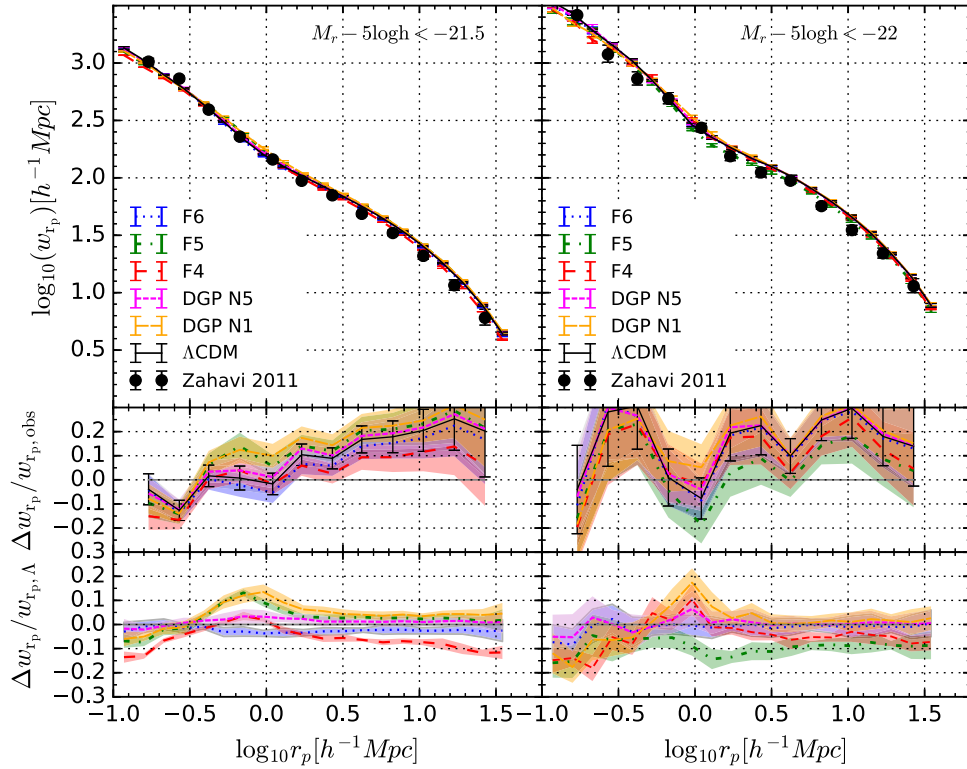


Figure 4. *Upper panels:* Projected two-point correlation function in the r -band calculated from the simulation-based mock catalogues of the different gravity models, using our SHAM results for the galaxy–halo connection. We split the catalogues into two sets of luminosity limits, $M_r - 5\log h < -21.5$ and $M_r - 5\log h < -22$ (left-hand and right-hand panels, respectively). The black circles with error bars show the results from SDSS DR7 (Zehavi et al. 2011). *Middle panels:* Relative differences of the model predictions with respect to the observational data points. The black error bars show the 1σ error in the observational results propagated to the differences with respect to the Λ CDM model. The shaded colour regions represent the variations estimated from the different realizations of each MG model. Note that though we observe differences up to 30 per cent in amplitude with respect to observations, the trends in the differences are similar for all the models, including the Λ CDM one. This means that the main differences with respect to observations are rather systematical for all the cases, and related mainly to the fact that we assumed no scatter in mocking the galaxies (see text). *Lower panels:* Relative differences of the MG models with respect to the Λ CDM. Note that the main differences of MG models with respect to the Λ CDM one is mostly within ~ 10 per cent in the left-hand panel and ~ 20 per cent in the right-hand panel.

are independent, we can fit the total mean occupation with five free parameters as

$$\langle N_{\text{tot}} \rangle = \langle N_{\text{cen}} \rangle + \langle N_{\text{sat}} \rangle. \quad (23)$$

The resulting best-fitting parameters for all the gravity models are shown in Fig. 5 with the solid lines for centrals and dotted lines for satellites. The colour code corresponds to the different MG models using the above equations. We report the best-fitting values of HOD parameters in Table 2. The maximum variation between the best-fitting values of the HOD parameters among the models are around ~ 40 per cent for M_1 ; ~ 35 per cent for M_{cut} ; ~ 26 per cent for M_{min} ; 10 per cent for α ; and 20 per cent for $\sigma_{\log M}$.

The bottom panel of Fig. 5 shows the differences w.r.t. the Λ CDM standard model as a function of halo mass. Here we observe that in the case of central galaxies, there is a difference around 10–50 per cent between MG models and Λ CDM, specially for $f(R)$ models at lower halo mass limits, $10^{12.5} h^{-1} < M_{200c} < 10^{13} M_{\odot} h^{-1}$. As for N5 and N1 models they are distinguishable from the standard Λ CDM in less than 5 per cent to 10 per cent at mass $10^{12.5} M_{\odot} h^{-1}$, respectively. The above results are not surprising as similar difference were noted in $M_r - V_{\text{max}}$ relation for central galaxies in Fig. 3. There, we noted that larger differences with respect to Λ CDM were observed in $f(R)$ gravity models than

in nDGP models. So, the results of HOD we have obtained are consistent with what we expected. The HOD of satellite galaxies is also different and depends on the gravity model that is used. Recall, that in our case we are using subhaloes as tracers of satellite galaxies as we have constrained separately the galaxy–halo connection for satellite galaxies. At high-mass limits, where satellite mean occupation number is dominated, we find that the total mean occupation numbers of galaxies of F4 model show a deficit of 10–20 per cent from the Λ CDM model at mass $10^{14.5} - 10^{15} M_{\odot} h^{-1}$ while rest of the MG models remains within 5 per cent difference.

The above results lead to a clear conclusion: HOD parameters depend on the gravity model employed. Thus, the use of HOD parameters derived from the Λ CDM cosmology and employed in MG simulations, would lead to biased conclusions from the analysis of the mean occupation of galaxies, as one can clearly see from Fig. 5. This will potentially reflect on the inferred galaxy clustering in MG models that will be in tension with observations. In other words, the differences in the HOD models described in the above figure should be interpreted as the result of the same degree of success in the galaxy clustering discussed in Fig. 4.

Independent constraints on the HOD of centrals and satellites may be an interesting possibility to search for some signature of MG.

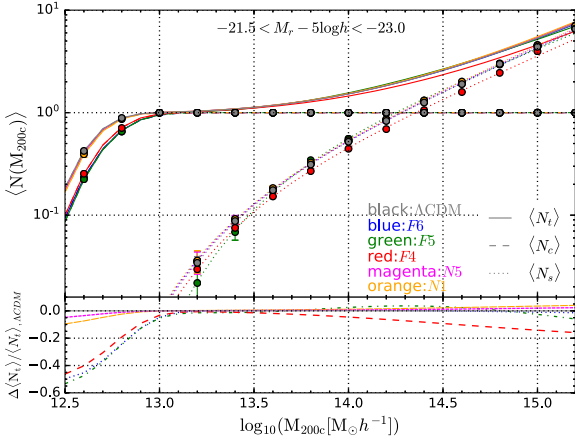


Figure 5. *Upper panel:* Mean galaxy occupation numbers as a function of host halo mass for central and satellite galaxies (filled circles) as estimated from our mock galaxy catalogues for the Λ CDM and MG models; the colour coding is shown inside the panel and it is the same as in Fig. 1. The dashed and dotted lines are best fits using the functional forms of mean occupation numbers for centrals (equation 22) and satellites (equation 21), respectively. The solid lines correspond to the total mean occupation numbers from the fit (equation 23). *Lower panel:* Relative differences of the fitted total mean occupation numbers between each MG model w.r.t. the Λ CDM. A sharp difference of 10–50 per cent is observed for the $f(R)$ models in the HOD corresponding to central galaxies in the mass range $10^{12.5} h^{-1} < M_{200c} < 10^{13} M_{\odot} h^{-1}$. For the nDGP models, the differences remain within 10 per cent for central occupation numbers and within ~ 5 per cent for satellite numbers. Similar differences in the satellite occupation numbers are seen for the $f(R)$ models, except for F4.

4.4 Measuring the dependence of the luminosity function on environment

As discussed in this paper, it is natural to expect some deviations from different statistics between gravity models. The most obvious is the demographics of dark matter haloes, namely, the velocity functions described in Section 3. Indeed, as shown in Fig. 1, we observe differences of approximately ~ 50 per cent between the velocity functions $\phi_V(V_{\max})$ of the different MG models analysed in the paper. Unfortunately, direct measurements of the velocity function from observations is not yet possible, thus, in this paper we look for other observable quantities that are natural projections of the halo velocity functions. The luminosity function is one of the most obvious observable distribution. While the observed total luminosity function is, by construction, the same in all our gravity models, so we expect that the observed differences in the halo velocity functions affect the dependence of the luminosity function on environment.

Thus, in this section we attempt to understand the effect of MG under different density environments; ranging from underdense regions like voids to highly dense regions like galaxy groups and clusters.

In the past, studies have already shown that the SHAM technique recovers the correct dependence of environmental density under the assumption of a Λ CDM universe (see e.g. Dragomir et al. 2018, and references therein). In particular, the recent work of Dragomir et al. (2018) showed that SHAM reproduces the correct dependence of the r -band galaxies luminosity functions for centrals and satellites of the SDSS DR7 from the Bolshoi-Planck simulation (Klypin et al. 2016; Rodríguez-Puebla et al. 2016a). Here we extend the study by Dragomir et al. (2018) to other gravity models to understand

whether the observed dependence of the luminosity function with environment is a simply tool to constrain gravity models.

In order to quantify environments that can be directly compared to observations, particularly to volume-limited samples, we define a *density-defining population* or DDP (Croton et al. 2005). Due to resolution limitations, for this work we define DDP galaxies within the absolute magnitude limit of $-21.5 > M_r - 5\log h > -22.5$. Our definition for the DDP population is a compromise between the lowest masses sample in our mock simulations and observations that can be done with current *galaxy surveys*, such as SDSS.

Among various existing methods to define local density environments (see e.g. Muldrew et al. 2012, for a review), we adopt the aperture-based methods where one measures the overdensities by counting the number of DDP galaxy neighbours, N_n , around each galaxy in the sample. Here, we are using an aperture of spheres of radius, $R_8 = 8h^{-1}$ Mpc and define the local density as

$$\rho_R = \frac{N_n}{4/3\pi R_R^3}. \quad (24)$$

In order to calculate the density contrast, we need to determine the mean number density of galaxies, $\bar{\rho}$. Based on the global r -band luminosity function we find that the number density at the range $-21.5 > M_r - 5\log h > -22.5$ is $\bar{\rho} = 5.824 \times 10^{-4} h^3 \text{ Mpc}^{-3}$. Then, for every galaxy in the mock we measure the density contrast within a sphere of radius R as

$$\delta_R = \frac{\rho_R - \bar{\rho}}{\bar{\rho}}. \quad (25)$$

Following previous studies (Croton et al. 2005; McNaught-Roberts et al. 2014; Dragomir et al. 2018), we focus our analysis mainly on spheres of radius $R = 8h^{-1}$ Mpc. This radius is optimal for sampling both underdense and overdense regions. None the less, we also use a large search radii, $R = 10h^{-1}$ Mpc, to amplify the signal in void regions. We expected that voids contain more information about different gravity models due to the nature of the screening mechanisms implemented on such MG models.

In Section 5 we will also discuss results based on $R = 10h^{-1}$ Mpc.

Next, we describe the procedure to determine the GLFs for different environments. Here we follow Dragomir et al. (2018) for determining the effective volume, $\mathcal{V}_{\text{eff}}(\delta_R)$ as the fraction of effective volume $f(\delta_R)$ sampled by the different environments in the simulation. In other words, the effective volume is given by $\mathcal{V}_{\text{eff}}(\delta_R) = f(\delta_R) \times V_{\text{sim}}$ where V_{sim} is the volume of the simulation. Hence, the r -band GLFs within a magnitude range of $M_r \pm \Delta M_r/2$ and $\delta_R \pm \Delta \delta_R/2$ density binning is given by

$$\phi_r(M_r, \delta_R) = \sum_{i=1}^N \frac{w_i(M_r \pm \Delta M_r/2, \delta_R \pm \Delta \delta_R/2)}{f(\delta_R) \times \Delta M_r \times V_{\text{sim}}}, \quad (26)$$

where w_i :

$$w_i = \begin{cases} 1 & \text{if } \delta_{r,i} \in (\delta_r \pm \Delta \delta_r/2) \text{ and } M_r \in (M_r \pm \Delta M_r/2) \\ 0 & \text{Otherwise} \end{cases}. \quad (27)$$

Following Dragomir et al. (2018), the fraction of effective volume, $f(\delta_R)$, as function of δ_R is measured by counting the number of DDP galaxy neighbours around a catalogue of random points:

$$f(\delta_R) = \frac{1}{N_r} \sum_{i=1}^{N_r} \Theta(\delta_{R,i}), \quad (28)$$

Table 2. Best-fitting values of the HOD parameters for satellite and central galaxies fitted to functions equations (21) and (22), respectively, based on the mock catalogues generated for all the models. Mass parameters are in units of $M_\odot h^{-1}$. Error bars on the HOD parameters correspond to 1σ , derived from the marginalized distributions. The HOD parameters vary from model to model; the largest differences among the constrained parameters are: ~ 40 per cent between F4 and F5 for M_1 ; ~ 35 per cent between F5 and N1 for M_{cut} ; ~ 26 per cent between Λ CDM and F5 for M_{min} ; 10 per cent between F6 and N1 for α ; and 20 per cent between Λ CDM and F5 for $\sigma_{\log M}$.

Models	$\log M_1$	$\log M_{\text{cut}}$	α	$\log M_{\text{min}}$	$\sigma_{\log M}$
Λ CDM	14.204 ± 0.012	13.403 ± 0.02	0.797 ± 0.021	12.627 ± 0.0002	0.201 ± 0.001
F6	14.184 ± 0.014	13.459 ± 0.017	0.739 ± 0.027	12.725 ± 0.003	0.24 ± 0.006
F5	14.156 ± 0.017	13.508 ± 0.018	0.762 ± 0.023	12.727 ± 0.003	0.236 ± 0.006
F4	14.300 ± 0.011	13.381 ± 0.013	0.79 ± 0.020	12.707 ± 0.002	0.228 ± 0.004
N1	14.195 ± 0.01	13.379 ± 0.023	0.80 ± 0.023	12.64 ± 0.0003	0.205 ± 0.001
N5	14.198 ± 0.01	13.402 ± 0.021	0.80 ± 0.021	12.633 ± 0.0002	0.203 ± 0.001

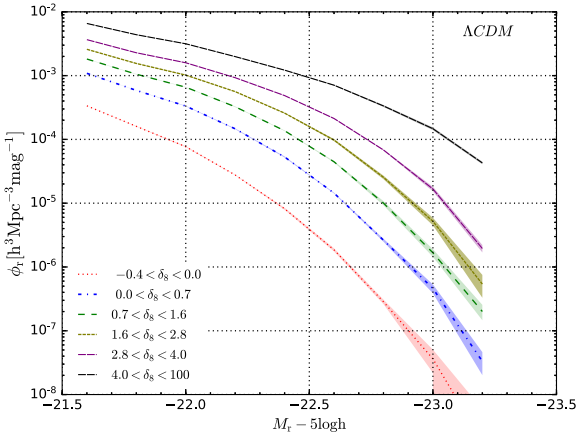


Figure 6. GLFs in the r band of all galaxies estimated from our mock galaxy catalogues for the Λ CDM model in six different density environments indicated inside the panel. Shaded regions represent 1σ standard deviation measured from their five realizations available.

where the function Θ counts the number of random points within the overdensity bin $\delta_R \pm \Delta\delta_R/2$:

$$\Theta(\delta_{R,i}) = \begin{cases} 1 & \text{if } \delta_{r,i} \in (\delta_r \pm \Delta\delta_r/2) \\ 0 & \text{Otherwise} \end{cases}. \quad (29)$$

Similar to equation (25), the local density contrast around each random point δ_r is calculated as

$$\delta_r = \frac{\rho_r - \bar{\rho}}{\bar{\rho}}. \quad (30)$$

We use a random catalogue that is ~ 4 times larger than the mock galaxy catalogues we created for all the gravity models, $\sim 4 \times 10^6$. We found that the variation in the fraction of effective volume measurements between the models with respect to Λ CDM is approximately within ~ 2 per cent.

In the following we present results in six density bins: $-0.4 < \delta_8 < 0.0$, $0.0 < \delta_8 < 0.7$, $0.7 < \delta_8 < 1.6$, $1.6 < \delta_8 < 2.8$, $2.8 < \delta_8 < 4.0$, and $4.0 < \delta_8$.

Finally, Fig. 6 shows the resulting dependence of the luminosity function on environment for the standard Λ CDM model. Note that as higher is the density environment bin the larger is the number of galaxies per comoving volume. Additionally, the GLF resembles a Schechter function, similarly to previous determinations for the Λ CDM model (Dragomir et al. 2018). While not shown here, we derive similar luminosity functions for all the gravity models. In the next section we will show just the differences with respect to the Λ CDM model.

5 GALAXY DISTRIBUTIONS AS A FUNCTION OF ENVIRONMENT IN THE DIFFERENT GRAVITY MODELS

In this section we present the resulting density distributions $\text{pdf}(1 + \delta_8)$ and the dependences of the luminosity functions on environment for all the MG models studied in this paper. We investigate whether the effects of environment from the MG models lead to differences on the luminosity functions, as different gravity models possess different screening mechanisms that should have some signatures under different environmental conditions.

5.1 The density distribution

We begin by describing the probability distribution of densities as measured for all the simulations. The left-hand panel of Fig. 7 shows the probability distribution of galaxy densities, $\text{pdf}(1 + \delta_8)$. Recall that densities were defined as the number of DDP neighbours within spheres of $R = 8h^{-1}$ Mpc. The bottom panel shows the difference with respect to the Λ CDM model. In general, Fig. 7 shows that the probability distribution for all the models are similar, though in more detail, some differences appear.

Fig. 7 shows that the largest significant differences between models appear for the low values of the overdensity, that is, for the void-like environments, $\delta_8 < 0$.

Moreover, there is a systematic trend among the models; F4, F5, and F6 predict up to 10 per cent for more low overdensities than the Λ CDM model, in contrast, the nDGP N1 and N5 models are slightly below the Λ CDM model but barely indistinguishable. This is in agreement with what we expect; for $f(R)$ models in the low-dense environments screening mechanisms are not that much effective (see e.g. Falck et al. 2015; Shi et al. 2017). For values of $\delta_8 \sim 1$, F4 predicts an excess of low overdensities compared to F5, F6, and the Λ CDM. Thus, the differences observed above clearly show the dependence of the chameleon mechanism with the parameter f_{R0} as well as with environment.

While in case of nDGP models, the Vainshtein mechanism seems to work efficiently, we observe no environmental effect which is consistent with the previous results of Falck et al. (2015). In denser environments, $\delta_8 > 4$, the above situation reverses and F4 and F6 models predict a lower fraction of cluster-like environments, by ~ 10 per cent, while F5 predicts a larger number of high-density environments, by ~ 20 per cent. Note that the excess of dark matter haloes observed in Fig. 1 are within the magnitude range definition of our DDP population. While, at this point, it is not clear how they would affect the definition of environment, one could argue that there is a non-negligible chance that the difference observed above are simply the result of including those haloes in our DDP

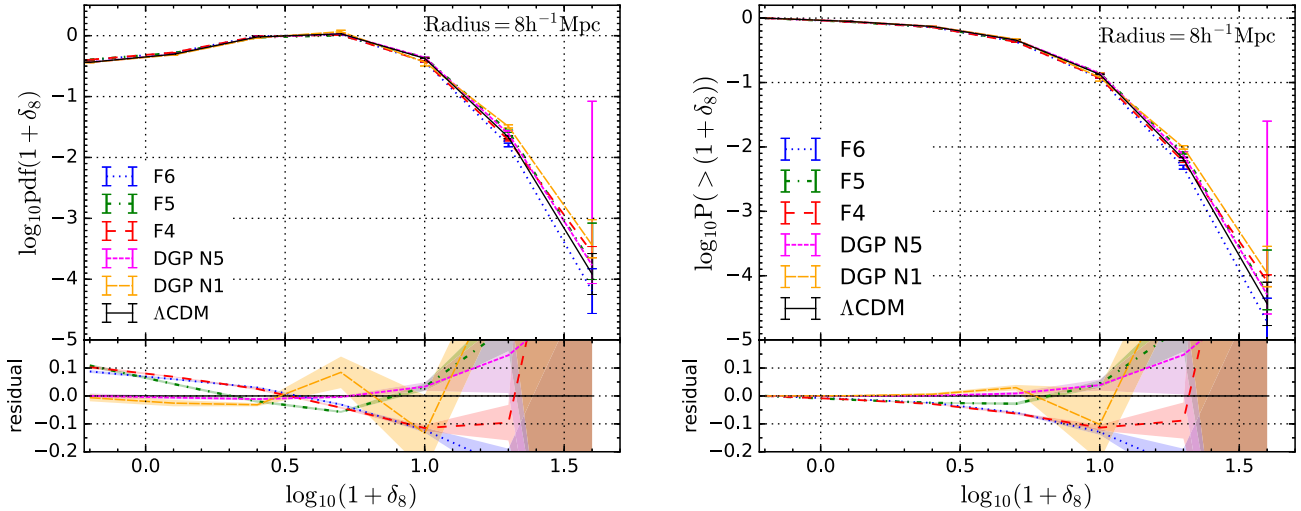


Figure 7. *Left-hand panel:* Differential $(1 + \delta_8)$ probability functions of all type of galaxies for all the models, where overdensity δ_8 is calculated within the sphere of radius $R = 8 \text{ Mpc } h^{-1}$. *Right-hand panel:* Cumulative $(1 + \delta_8)$ probability function. The binning is done with 0.3 dex.

definition. We will discuss further this point in Section 6. Finally, as for nDGP N1, this model makes excursions around the ΛCDM expectations but at the largest density environments it predicts more structures with high δ_8 , > 20 per cent. But for the nDGP N5 we observe that is consistent with the ΛCDM at all density environments and it is difficult to conclude whether there is some environmental dependence for these models due the large errors in our determinations.

The right-hand panel of Fig. 7 shows the cumulative probabilities $P(>\delta_8 + 1)$, while the bottom panels present the residuals with respect to the ΛCDM model. While the trends observed in this figure are well understood from the density probability distribution (left-hand panel), Poissonian errors have a lower impact in $P(>\delta_8 + 1)$, which could be used for constraining gravity models.

5.2 The dependence of the luminosity function on environment in modified gravity models

As discussed above, we find evidence that the resulting galaxy density fields are different for different gravity models as well as for their screening mechanisms. Next, we study the effect of the gravity models on the dependence of the luminosity function with environment.

The main goal of this work is to quantify the differences on the dependence of the r -band GLF with environment for all the gravity models studied here. Recall that Fig. 6 shows the GLFs under different environments (δ_8 values) for the standard ΛCDM model.

The resulting differences of the respective GLFs in the different gravity models w.r.t. the ΛCDM model are shown in Fig. 8. Each panel corresponds to the different environments, ranging from void-like structures, $-0.4 < \delta_8 < 0$, to clusters-like environments, $\delta_8 > 4$. The shaded regions show the 1σ standard deviation from the 5 realizations for the F6 and N5 gravity models. We only present uncertainties in F6 and N5 to avoid overcrowding as they are expected to be the closer in nature to the ΛCDM model. We note, however, that we find similar uncertainties for all the other gravity models. The solid vertical line in each panel shows the threshold limit, $M_r < -22.8$, below which we cannot trust the results due to sampling variance in the simulations. In Appendix B,

we show that when recovering the cumulative luminosity function from the simulations, uncertainties due to sampling variance, ~ 5 – 10 per cent, become relevant for bright galaxies. Thus, as a conservative limit we use the threshold limit of $M_r < -22.8$, as shown in Fig. B1.

In Fig. 8, we observe that overall all MG models considered here deviate from the standard ΛCDM model at *all density bins*. This is especially true at low-density environments where we find differences of the order of ~ 10 per cent in some of the models, where the screening mechanisms are not efficient. At the high-density environments, where the screening mechanisms are expected to be more efficient, the differences are around ~ 5 per cent.

In general the F4 and F6 models predict a higher number of galaxies for all magnitudes and for most of the environments. This situation is inverted at the highest density bin at which they predict a lower amplitude for low-luminosity galaxies but approaches to the ΛCDM model at the bright end. The model F5 is closer to the ΛCDM model within $0 \lesssim \delta_8 \lesssim 4$. At the lowest overdensity bin it seems to be higher than the ΛCDM model but this depends on luminosity, galaxies with $M_r \sim -22.5$ have a maximum deviation of ~ 9 per cent from the ΛCDM model. At the largest overdensity bin, $\delta_8 > 4$, F5 predicts ~ 9 per cent more galaxies at $M_r \sim -21.9$ but it is similar to the ΛCDM model for brighter galaxies. As for nDGPs models, both N5 and N1, are almost indistinguishable to the ΛCDM model for magnitudes below $M_r \sim -22.2$. None the less, we find some deviations for brighter galaxies with differences around 8–10 per cent and 10–15 per cent respectively for N5 and N1 at a fixed luminosity $M_r \sim -22.7$.

The above trends are surprising and unexpected, specially for the F4, F5, and F6 models. In fact, the F4 model is expected to deviate significantly from the ΛCDM , followed by F5 and F6 due to the chameleon screening mechanism. Note, however, that in Fig. 1 (see also Fig. A1) we showed that the differences of the F4, F5, and F6 models w.r.t. ΛCDM depend on the halo velocity (mass). Moreover we showed that for haloes with $V_{\text{max}} \sim 630 \text{ km s}^{-1}$ (corresponding to $M_r \sim -22.2$ in terms of galaxies) there is a maximum excess of ~ 50 per cent of haloes for the F5 model. As before, we do not see the above features in Fig. 8. In the case of the nDGP models, N5 was expected to be closer to the ΛCDM than N1, something that we notice. However, it is not clear why they are below the predictions

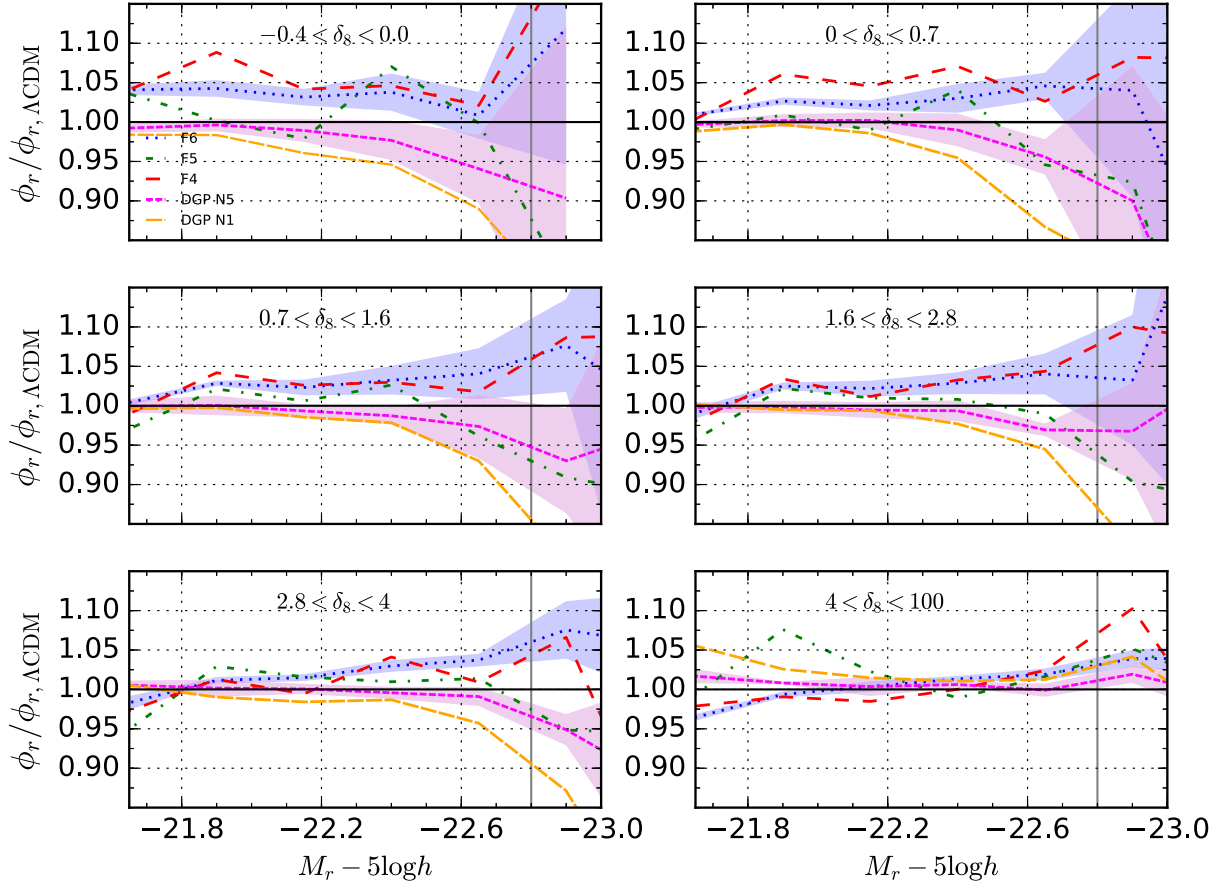


Figure 8. GLFs in the r band of each one of the MG models considered here with respect to the Λ CDM GLF in six different density environments determined within the sphere of $R = 8 \text{ Mpc } h^{-1}$. The overdensities δ_8 decrease from upper left to the right lower corners. The resulting GLFs are the mean of all the available simulation realizations. The shaded regions show the respective error propagation from the standard deviation calculated from the realizations available for the F6 and N5 MG models, which are the closest in nature to the Λ CDM from the theoretical background. The error propagation for the other models is not shown to avoid overcrowding in the figures. The solid vertical line shows the threshold limit below which we cannot trust on the results due to uncertainties, coming from various factors, e.g. SHAM technique, estimation of the f_{sat} function, etc.

from the Λ CDM model for brighter galaxies. In the next section we discuss on the possible origin of the above tensions.

Finally, despite of the details discussed above, Fig. 8 shows that the differences in halo distributions among the different gravity models are projected somehow in the dependence of the GLFs on environment in such a way that is possible to distinguish between the different models by means of observations.

As noted previously, the most significant differences of MG models w.r.t. the Λ CDM standard model is at low-density environments, $\delta_8 < 1$. While there are hints of some differences at high-overdensity bins, most of the models are very close to the Λ CDM. This is actually expected due to the enhancement of the screening mechanism in the different models that allows to recover GR in high-density regions.

The above trend with environment gives an idea on how does the MG affects the GLFs at different environments, providing thus a valuable tool for distinguishing MG effects from Λ CDM. Moreover, based on our results, we propose that the dependence of the GLF on environment can be used to constrain screening mechanisms along with the gravity models.

Similarly to Fig. 8, Fig. 9 shows the dependence of the luminosity function with environment w.r.t. Λ CDM but this time using an aperture sphere of $R = 10 \text{ Mpc } h^{-1}$. Note that using larger apertures would tend to oversample voids and thus increasing the effects of

the fifth force from the MG models. None the less, we observe approximately the same trends as in the case of spheres of $R = 8 \text{ Mpc } h^{-1}$. Thus increasing the aperture radius do not significantly change our conclusions.

6 DISCUSSION

In the non-linear regime of structure formation, different screening mechanisms predict that dark matter particles will cluster differently. In consequence, as it has been shown by previous studies (see e.g. Falck et al. 2015), haloes themselves cluster differently as well. In this paper, we study the environmental dependence of the GLFs as predicted by different gravity models. Here we use two different class of MG models and their screening mechanism, the $f(R)$ (Hu & Sawicki 2007) and the nDGP (Dvali et al. 2000), in order to build mock galaxy catalogues and their corresponding galaxy density field.

In the preceding section, we conclude that the dependence of the GLF on environment is a valuable tool for constraining the screening mechanisms in addition of the MG models. None the less, we noted that the trends in the GLFs were counter-intuitive to what theoretically is expected, see Fig. 1 from Section 3, specially for the F4, F5, and F6 models. There, we discussed that the chameleon screen mechanism tends to produce an excess of abundance of dark

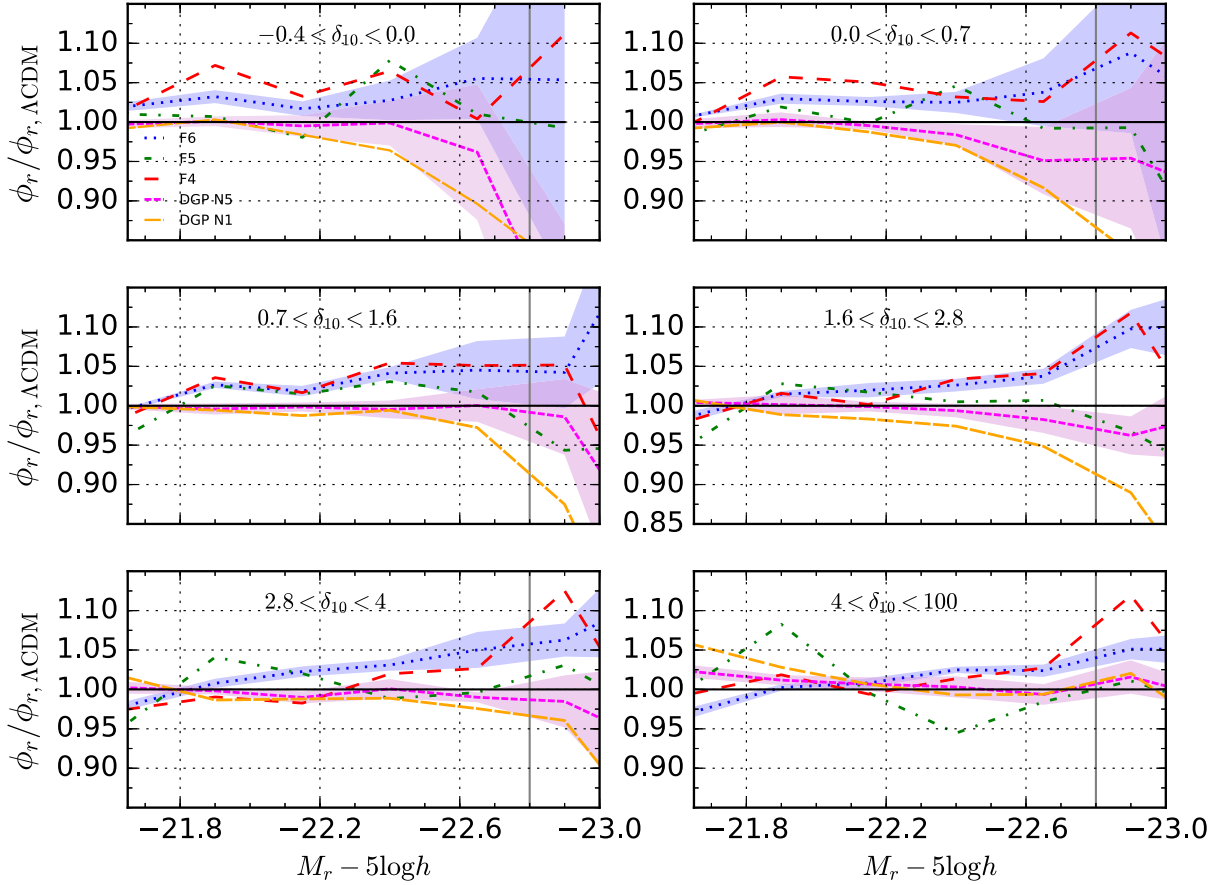


Figure 9. Same as Fig. 8 but for a sphere of $R = 10 \text{ Mpc } h^{-1}$. By varying from 8 to $10 \text{ Mpc } h^{-1}$, the radius of the sphere where the overdensities are measured, we do not see major differences for the MG models throughout all the different environments.

matter haloes around some characteristic velocity/mass that depends on the present day value of the scalaron field (Li & Efstathiou 2012). In the halo velocity/mass range of the suite of N -body simulations we are employing for this paper, we observe that the maximum excess of dark matter haloes for the F5 model is of ~ 50 per cent, w.r.t. ΛCDM , at $V_{\text{max}} \sim 600 \text{ km s}^{-1}$, which corresponds to haloes with $M_{200c} \sim 6 \times 10^{13} M_{\odot}$; see Figs 1 and A1, respectively. On the other hand, F6 and F4 models show an excess of dark matter haloes respectively of ~ 20 per cent (at low velocities/masses) and more than 100 per cent (at high velocities/masses). In the case of the nDGP models, N1 predicts an excess of haloes at the high-mass end while N5 is almost indistinguishable from the ΛCDM . Further, we discuss why we do not recover the above trends into the predicted GLFs.

Fig. 10 presents the dependence of the halo velocity functions for the various MG models w.r.t. ΛCDM on the environment. Note that we employed the same definition of environments, δ_8 , derived for their host galaxies from the previous section. The halo velocity functions were derived using the same methodology as described in Section 4.4. Fig. 10 shows that the trends observed in Fig. 1 are replicated in all the environments. As expected, at the low-density environments the effects of the fifth force are more relevant leading to a larger differences w.r.t. ΛCDM than at the high-density environments, where the fifth force is suppressed and the screening mechanisms are more efficient. Note, however, that even in the highest overdensity bin we do observe similarities with Fig. 1. Naively, the above signatures are what we would expect to be printed

in the dependence of the GLFs with environment. Therefore, we discard that the methodology employed in Section 4.4 is responsible for erasing the features observed in Fig. 1. Moreover, we also discard that choosing our DDP population within the magnitude range at which the F5 model shows an excess of haloes, is not introducing an extra source of bias between the F5 and the other models. Next, we investigate whether the differences on the $V_{\text{max}}-M_r$ relations are responsible for the counterintuitive results of the dependence of the GLFs with environment.

In this paper we derived the $V_{\text{max}}-M_r$ relationship via SHAM under the assumptions of zero scatter and *separately* for all the gravity models. Thus, in this approach, haloes with identical V_{max} will host galaxies with identical luminosities M_r , no matter what their environmental density is. In other words, the $V_{\text{max}}-M_r$ relation is independent of environment. Assuming that we have a model for the dependence of the velocity function with environment $\phi_V(V_{\text{max}}|\delta_8)$ and using the universality of the $V_{\text{max}}-M_r$ relation, we can thus derive the dependence of the GLF with environment as

$$\phi_r(M_r|\delta_8) = \phi_V(V_{\text{max}}(M_r)|\delta_8) \left| \frac{d \log V_{\text{max}}(M_r)}{d M_r} \right|. \quad (31)$$

Notice that the above equation is simply the differential form of SHAM. When examining equation (31), it clearly shows that when two models have different $V_{\text{max}}-M_r$ relationships, the observed features from these models in their corresponding velocity functions

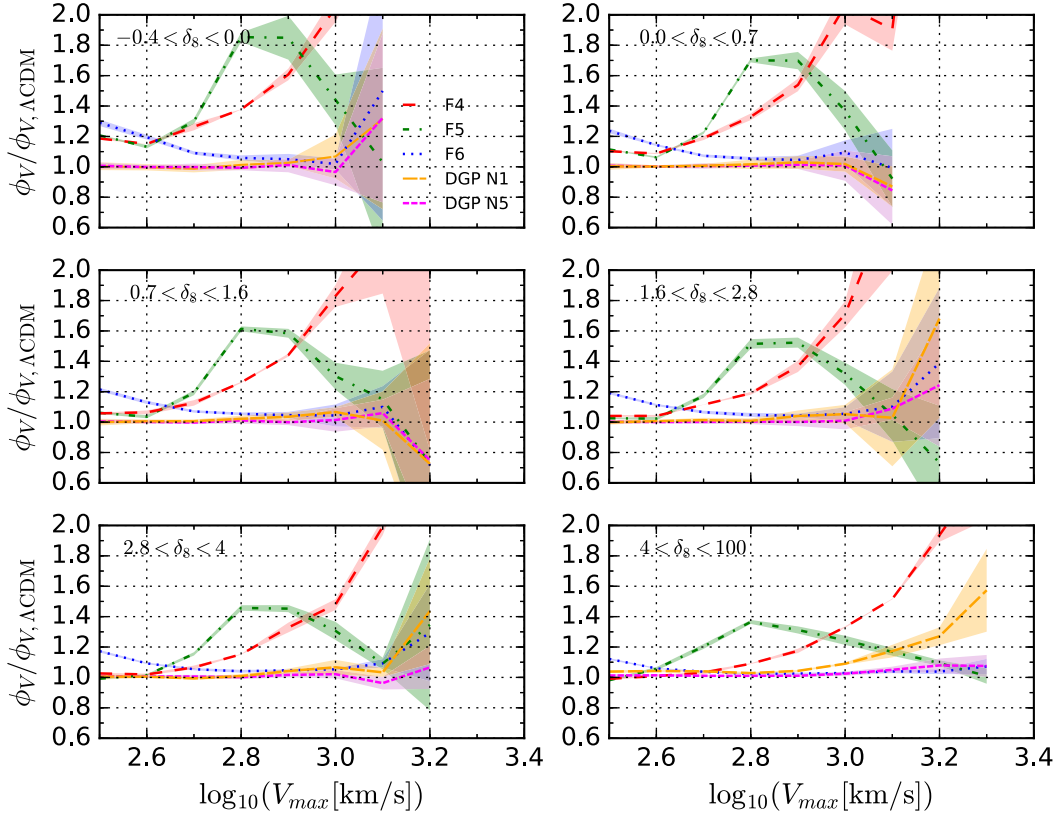


Figure 10. Variations with environment the halo V_{\max} functions of the MG models with respect to the Λ CDM. The shaded areas represent the error propagated from the standard deviations of all the available realizations. Some of the trends seen in Fig. 1 for haloes in all the environments are enhanced in the low-density environments. While in high-density environments the fifth force is expected to be suppressed but we observe differences between screening models and similar features to Fig. 1.

will not be directly projected into their GLFs. This is due to the non-trivial relationship between galaxies (magnitudes) and haloes (velocities), depending strongly not only in the functional forms of the $V_{\max} - M_r$ relations but also on their slopes.

To understand the above, imagine that we want to compare two models with different $V_{\max} - M_r$ relations such that Model 1 has a higher amplitude than Model 2. That is, at a fixed V_{\max} the Model 1 host brighter galaxies than the Model 2. Equivalently, at a fixed luminosity we find that $V_{\max,1} < V_{\max,2}$, where the subscripts ‘1’ and ‘2’ indicate the models. Equation (31) shows that when comparing two models with identical magnitudes (this is actually our situation in Fig. 8 where we are comparing different models at a fixed magnitude) the differences observed in Figs 1 and 10, at a fixed V_{\max} , will project differently into the GLFs, due to the shift in the halo velocities by simply fixing the galaxy magnitudes. This could explain the observed trends from Fig. 8. The mapping between V_{\max} and M_r would perhaps in some cases compress, stretch, squash or just shift, or a combination of all of them, the features observed in Figs 1 and 10.

We test the above idea, by choosing one (from the five realizations) of the simulations for each gravity models and by employing equation (31) combined with our determinations of $\phi_V(V_{\max}|\delta_8)$, similarly to Fig. 10, and the $V_{\max} - M_r$ relations for all the gravity models, see Fig. 3. The resulting GLFs as a function of environment, $\phi_r(M_r|\delta_8)$, are shown in Fig. C1 from Appendix C. Note that our results based on SHAM, equation (31), are very similar to the direct measurements from the simulations. Next we study the ratio w.r.t. Λ CDM.

Similarly to Fig. 8, Fig. 11 shows the dependence of the GLF with environment from equation (31) w.r.t. Λ CDM. Observe that we are replicating the same features in both figures. The above confirms that the differences in the $V_{\max} - M_r$ relations of the gravity models are responsible for the intriguing and counter-intuitive results from Section 5.2. The differences within 10 per cent among the models are being observed in the GLFs under different environments with the fact that different gravity models lead to have different $M_r - V_{\max}$ relationships.

We end this section by emphasizing that the features derived for the distributions of dark matter haloes would not necessarily map directly into their host galaxies. As we have discussed, the mapping between galaxies and dark matter haloes is not trivial and it depends on the gravity model. In order to compare predictions from different gravity models, one should use the correct galaxy–halo connection for each model. Otherwise, one would be prone to draw wrong conclusions on the real viability of one model over the others. That would be the case when using HOD parameters derived from the Λ CDM model but employed in other MG models, see also the discussion in Section 4.3.

7 SUMMARY AND CONCLUSIONS

We have studied the differences of several halo and galaxy distributions predicted within the context of two classes of MG models and their respective screening mechanisms. We explored (i) the $f(R)$ model of Hu & Sawicki (2007) with $n = 1$ and three different $|f_{R0}|$ values: $F6 = 10^{-6}$, $F5 = 10^{-5}$, and $F4 = 10^{-4}$ (see equation 6), and

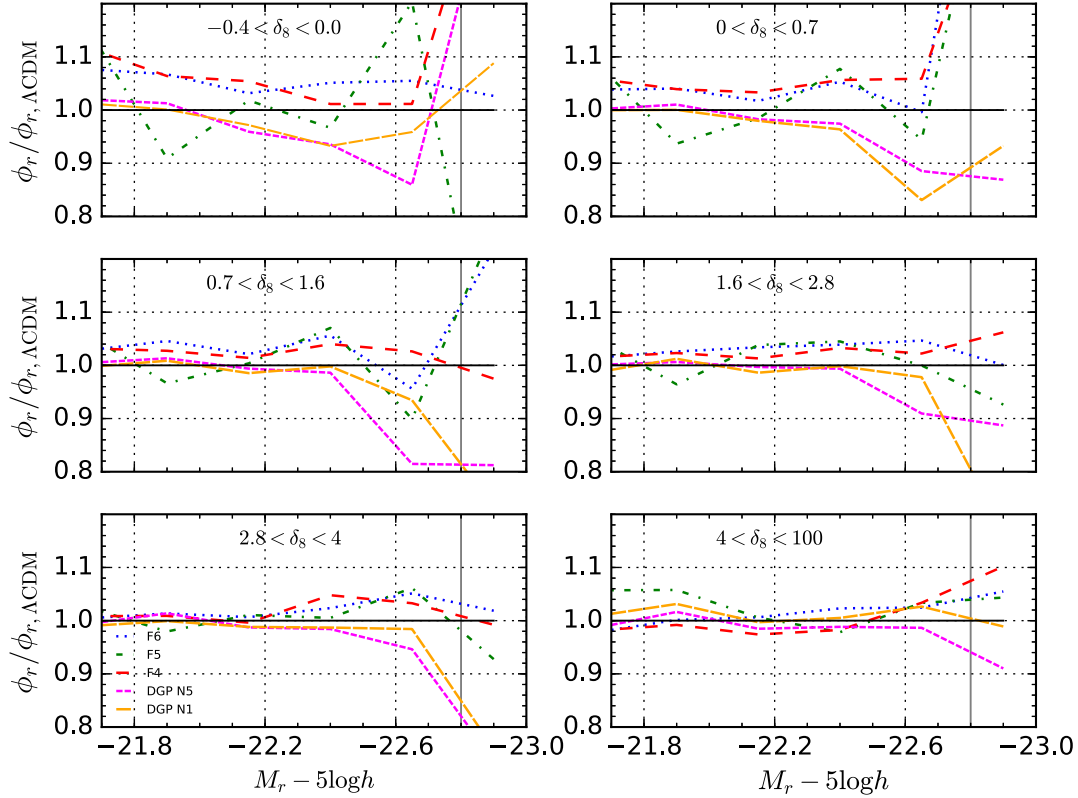


Figure 11. As Fig. 8 but for the GLFs calculated from the respective halo V_{max} functions as a function of environment, $\phi_V(V_{\text{max}}|\delta_8)$, and the $M_r - V_{\text{max}}$ relation (see equation 31). Only one realization for each model has been used for this plot. The results in this plot are similar to those obtained directly from the mock catalogues, shown in Fig. 8.

(ii) the normal branch of Dvali et al. (2000) (nDGP) Braneworld model, with $r_c H_0/c = 5$ and 1.0, denoted respectively by N5 and N1. We used a large suite of high-resolution N -body cosmological simulations for these MG models and for the standard ΛCDM model. The simulations were presented in Li et al. (2012, 2013). Each model has five different realizations, which are ran using slightly different random phases for the initial conditions, except for F4 model that has only two realizations. We used these realizations to determine uncertainties from sampling variance.

The dark matter (sub)haloes were populated with galaxies by means of the SHAM. For the SHAM, we used the halo maximum circular velocity (V_{max}) function from the simulations and the r -band GLF from SDSS. As the result, and following Rodríguez-Puebla et al. (2012), we obtained the $M_r - V_{\text{max}}$ relationships for both the central and satellite galaxies (haloes and subhaloes). These relationships connect galaxies with (sub)haloes, in such a way that the spatial clustering of galaxies at different r -band luminosities can be measured in the simulations. For all the gravity models studied here, the predicted projected two-point correlation functions (Fig. 4) agree with observational determinations, with differences at some scales up to ~ 30 per cent, and with the deviations from them being similar for all the models. This shows that the employed SHAM method is relatively robust and that the systematic differences with observations do not introduce biases in our further comparative analysis among the different gravity models.

Further, we characterized the galaxies in the simulations by their environmental density, δ_8 , by counting neighbours in spheres of $R = 8 \text{ Mpc } h^{-1}$, and calculated the GLFs as a function of environment with the aim of exploring whether the dependence of the GLF on environment changes among the differ-

ent gravity models, providing possible observational signatures to constrain them. Our main results and conclusions are as follows:

(i) The V_{max} function, $\phi_V(V_{\text{max}})$, and the halo mass function, $\phi_h(M_{200c})$, for haloes and subhaloes depend on the gravity models. The F4 model predicts ~ 50 per cent more haloes and subhaloes than the ΛCDM model around $V_{\text{max}} \sim 1000 \text{ km s}^{-1}$, the difference increasing for larger values of V_{max} . For the F5 model, there is an excess of haloes/subhaloes w.r.t. the ΛCDM model up to 50 per cent at the V_{max} range of 400–1000 km s^{-1} . We observe qualitatively similar differences in the halo mass function but with smaller amplitude.

This is because the haloes in these $f(R)$ models are also more concentrated (higher V_{max} values for a given halo mass), so that besides the abundance excess, they have larger velocities than in the ΛCDM model.

These differences are expected due to the inefficiency of the screening mechanism for these models in the relevant V_{max} /mass regime. On the other hand, the F6 model predictions are similar to those of the ΛCDM model due to the strong screening mechanism acting on the V_{max} /mass regime explored in the simulations. Finally, the N1 and N5 models remain indistinguishable from the ΛCDM model throughout most of the V_{max} /mass ranges due to the effective suppression of the fifth force under the Vainshtein screening method employed by these models.

(ii) The obtained $M_r - V_{\text{max}}$ relationships of central and satellite galaxies vary among the various gravity models. The differences are not larger than ~ 1 per cent, which correspond to differences of ~ 0.2

mag in M_r . These results are mainly consequence of the differences among the maximum circular velocity functions reported above.

(iii) The variation of the M_r – V_{\max} relationships with gravity models affects the results on the halo occupation distributions, HOD. The maximum variation in the best fit values of the HOD parameters among the different gravity models are around ~ 40 per cent for M_1 ; ~ 35 per cent for M_{cut} ; ~ 26 per cent for M_{min} ; 10 per cent for α ; and 20 per cent for $\sigma_{\log M}$. We observe differences in the halo occupation numbers between the $f(R)$ models and the Λ CDM one up to 50 per cent. The major differences (a deficit of centrals) are at $M_{200c} < 10^{13} M_{\odot} h^{-1}$, and also at the high-mass end for the F4 model. For the nDGP models the differences are below the 10 per cent. We stress that since the HOD numbers depend on the MG, it is not correct then to apply Λ CDM-based HOD parameters for seeding galaxies in haloes from simulations for the MG models.

(iv) The galaxy overdensity distribution, $\text{pdf}(1 + \delta_8)$, varies with the gravity model. For the F4, F5, and F6 models, there is a 10 per cent excess of void-like regions compared to the Λ CDM. In contrast, at the high-end of the $(1 + \delta_8)$ distribution, for F4 and F6, there is a ~ 10 per cent deficit of high-density environments but for F5 there is a ~ 20 per cent excess of high-density environments. For the DGP N1 and N5 models, the overdensity distributions are similar to those predicted for Λ CDM, excepting at the high-density end, where the variance is large.

(v) The various gravity models analysed here predict a different dependence of the GLF with environment. The most significant difference w.r.t. the Λ CDM is at the low-density environments, $\delta_8 \lesssim 1$. The F4 model has an excess of ~ 5 – 10 per cent at the lowest density bins and at all luminosities, followed by the F6 model. Contrary to the naive expectation, F5 is closer to the Λ CDM prediction than F6 along with some fluctuation in F5. The DGP N5 and N1 models are closer to the Λ CDM model for lower luminosity galaxies but we observe a deficit of high-luminosity galaxies in almost all the environments, ~ 9 per cent and ~ 12 per cent for N1 and N5 models, respectively.

(vi) We have discussed the counterintuitive results on the expected dependence of the GLFs with environment and screening mechanisms, specially for the sequence of models F6, F5, and F4. The dependence of the halo V_{\max} function with environment, $\phi_V(V_{\max}|\delta_8)$, is mapped into a dependence of the GLFs by environment, $\phi_r(M_r|\delta_8)$, through the V_{\max} – M_r relationship (equation 31) in a very non-linear way because the latter has a non-trivial shape that varies among the different gravity models and their screening mechanisms. The effects of the shape and differences in the V_{\max} – M_r relations could result in some cases in the compression, stretch, squash or just shift (or a combination of all of them) of the features produced by the screening mechanisms in the $\phi_V(V_{\max}|\delta_8)$ function.

Our results are in general consistent with the findings of Hernández-Aguayo et al. (2018), where the authors studied the impact of $f(R)$ gravity on galaxy clustering using marked correlation functions. In the marked correlations approach, one gives a ‘weight’ or ‘mark’ to each galaxy as a function of the environment (Sheth, Connolly & Skibba 2005), with the idea to up-weight low-density regions to boost the MG signal in galaxy clustering (White 2016). Hernández-Aguayo et al. (2018) found that up-weighting low- and intermediate-density regions it is possible to find measurable differences between $f(R)$ gravity models and GR (Λ CDM). This result is similar to the differences found here in the GLFs as a function of δ_8 and δ_{10} (see Figs 8 and 9), especially in the bins: $-0.4 < \delta_{8/10} < 0$, $0 < \delta_{8/10} < 0.7$ and $0.7 < \delta_{8/10} < 1.6$.

Our simple approach of analysing the GLFs under different environment can provide a complimentary test to other existent non-linear observables such as galaxy clustering redshift-space distortions (Vlah & White 2019; Hernández-Aguayo et al. 2019), weak lensing measurements (Shirasaki, Hamana & Yoshida 2015), cluster abundances (Cataneo et al. 2015), and the marked correlation functions (White 2016; Hernández-Aguayo et al. 2018). Indeed, our measurements quantify the effect of MG models and their screening effect as a function of galaxy environment, especially in the low- (void like) and high- (cluster like) density regions. Perhaps, combining various observables will improve the constraints on the different MG models. In addition, the fact that the HOD parameters depend on the gravity model, as we have found, observational results on the conditional luminosity/stellar mass functions (e.g. Yang et al. 2007) would be helpful for constraining the models.

Finally, this paper is the first on a series for examining the effects of the screening mechanism of the MG models at the level of galaxy properties, particularly the dependence of the GLF with environment. While our results show that it is, in principle, possible to use the observed GLFs to establish limits or to constrain MG models, even though we have ignored errors from observations. We are currently developing realistic galaxy mocks by including random errors from magnitude and redshift determinations in order to test the viability of using the above idea with current facilities such as the SDSS and DES or even with future surveys such as DESI. In addition, here we mainly focused on the r -band magnitude but the analysis can be easily extended to other bands or even at the level of galaxy stellar mass. Considering the robustness of the SHAM method mentioned before, performing HOD directly on MG models is our next future plan.

ACKNOWLEDGEMENTS

NCD thanks Hector Ibarra and A.R. Calette for useful comments and discussions. NCD acknowledges support from a DGAPA-UNAM post-doctoral fellowship and the Mexican National Council of Science and Technology (CONACyT) Fronteras de la Ciencia grant 281. ARP and VAR acknowledges support from UNAM PAPIIT grant IA104118 and from the CONACyT ‘Ciencia Basica’ grant 285721. OV acknowledges support from UNAM PAPIIT grant IN112518. CHA acknowledges support from the CONACyT through grant No. 286513/438352. Some of the simulations used in this worked were run on the OKEANOS supercomputer hosted by the Interdisciplinary Centre for Mathematical and Computational Modelling, University of Warsaw, kindly made available to us by Wojciech Hellwing.

REFERENCES

- Aghamousa A. et al., 2016, preprint ([arXiv:1611.00036](https://arxiv.org/abs/1611.00036))
- Barreira A., Bose S., Li B., 2015, *J. Cosmol. Astropart. Phys.*, 1512, 059
- Barreira A., Sánchez A. G., Schmidt F., 2016, *Phys. Rev. D*, 94, 084022
- Baugh C. M., 2006, *Rep. Prog. Phys.*, 69, 3101
- Beaton R. L. et al., 2016, *ApJ*, 832, 210
- Behroozi P. S., Wechsler R. H., Wu H.-Y., 2013a, *ApJ*, 762, 109
- Behroozi P. S., Wechsler R. H., Conroy C., 2013b, *ApJ*, 770, 57
- Behroozi P., Wechsler R., Hearin A., Conroy C., 2019, preprint ([arXiv:1806.07893](https://arxiv.org/abs/1806.07893))
- Blanton M. R. et al., 2005, *AJ*, 129, 2562
- Bose S., Hellwing W. A., Li B., 2015, *J. Cosmol. Astropart. Phys.*, 1502, 034
- Bose S., Li B., Barreira A., He J.-h., Hellwing W. A., Koyama K., Llinares C., Zhao G.-B., 2017, *J. Cosmol. Astropart. Phys.*, 1702, 050

- Burrage C., Sakstein J., 2016, *J. Cosmol. Astropart. Phys.*, 1611, 045
- Campbell D., van den Bosch F. C., Padmanabhan N., Mao Y.-Y., Zentner A. R., Lange J. U., Jiang F., Villarreal A., 2018, *MNRAS*, 477, 359
- Capozziello S., Fang L. Z., 2002, *Int. J. Mod. Phys. D*, 11, 483
- Carroll S. M., 2001, *Living Rev. Rel.*, 4, 1
- Cataneo M. et al., 2015, *Phys. Rev. D*, 92, 044009
- Chiba T., 2003, *Phys. Lett. B*, 575, 1
- Cognola G., Elizalde E., Nojiri S., Odintsov S. D., Sebastiani L., Zerbini S., 2008, *Phys. Rev. D*, 77, 046009
- Collett T. E. et al., 2018, *Science*, 360, 1342
- Conroy C., Wechsler R. H., Kravtsov A. V., 2006, *ApJ*, 647, 201
- Croton D. J. et al., 2005, *MNRAS*, 356, 1155
- De Felice A., Tsujikawa S., 2010, *Living Rev. Rel.*, 13, 3
- Dolgov A. D., Kawasaki M., 2003, *Phys. Lett. B*, 573, 1
- Dragomir R., Rodríguez-Puebla A., Primack J. R., Lee C. T., 2018, *MNRAS*, 476, 741
- Dvali G., Gabadadze G., Porrati M., 2000, *Phys. Lett. B*, 485, 208
- Falck B., Koyama K., Zhao G.-B., 2015, *J. Cosmol. Astropart. Phys.*, 1507, 049
- Faraoni V., 2006, *Phys. Rev. D*, 74, 104017
- Firmani C., Avila-Reese V., 2000, *MNRAS*, 315, 457
- Freedman W. L., 2017, *Nat. Astron.*, 1, 0121
- Frenk C. S., White S. D. M., 2012, *Ann. Phys., Lpz.*, 524, 507
- He J.-H., Li B., Baugh C. M., 2016, *Phys. Rev. Lett.*, 117, 221101
- Hernández-Aguayo C., Baugh C. M., Li B., 2018, *MNRAS*, 479, 4824
- Hernández-Aguayo C., Hou J., Li B., Baugh C. M., Sánchez A. G., 2019, *MNRAS*, 485, 2194
- Hinshaw G. et al., 2013, *ApJS*, 208, 19
- Hu W., Sawicki I., 2007, *Phys. Rev. D*, 76, 064004
- Jain B., Vikram V., Sakstein J., 2013, *ApJ*, 779, 39
- Joyce A., Jain B., Khoury J., Trodden M., 2015, *Phys. Rep.*, 568, 1
- Khoury J., 2010, preprint (arXiv:1011.5909)
- Khoury J., Weltman A., 2004, *Phys. Rev. D*, 69, 044026
- Klypin A., Yepes G., Gottlöber S., Prada F., Heß S., 2016, *MNRAS*, 457, 4340
- Koyama K., 2016, *Rep. Prog. Phys.*, 79, 046902
- Koyama K., Silva F. P., 2007, *Phys. Rev. D*, 75, 084040
- Kravtsov A. V., Berlind A. A., Wechsler R. H., Klypin A. A., Gottlöber S., Allgood B., Primack J. R., 2004, *ApJ*, 609, 35
- Li B., Efstathiou G., 2012, *MNRAS*, 421, 1431
- Li B., Zhao G.-B., Teyssier R., Koyama K., 2012, *J. Cosmol. Astropart. Phys.*, 1201, 051
- Li B., Zhao G.-B., Koyama K., 2013, *J. Cosmol. Astropart. Phys.*, 1305, 023
- Linder E. V., 2009, *Phys. Rev. D*, 80, 123528
- Lombriser L., 2014, *Ann. Phys., Lpz.*, 526, 259
- Martinelli M., Melchiorri A., Amendola L., 2009, *Phys. Rev. D*, 79, 123516
- McNaught-Roberts T. et al., 2014, *MNRAS*, 445, 2125
- More S., van den Bosch F., Cacciato M., More A., Mo H., Yang X., 2013, *MNRAS*, 430, 747
- More S., van den Bosch F., Cacciato M., More A., Mo H., Yang X., 2014, *J. Phys. Conf. Ser.*, 484, 012042
- Mo H. J., Mao S., White S. D. M., 1998, *MNRAS*, 295, 319
- Muldrew S. I. et al., 2012, *MNRAS*, 419, 2670
- Nojiri S., Odintsov S. D., 2003, *Phys. Rev. D*, 68, 123512
- Perlmutter S. et al., 1999, *ApJ*, 517, 565
- Planck Collaboration XIII, 2016, *A&A*, 594, A13
- Planck Collaboration VI 2018, preprint (arXiv:1807.06209)
- Prunet S., Pichon C., Aubert D., Pogosyan D., Teyssier R., Gottloeber S., 2008, *ApJS*, 178, 179
- Ratra B., Peebles P. J. E., 1988, *Phys. Rev. D*, 37, 3406
- Reddick R. M., Wechsler R. H., Tinker J. L., Behroozi P. S., 2013, *ApJ*, 771, 30
- Riess A. G. et al., 1998, *AJ*, 116, 1009
- Riess A. G. et al., 2016, *ApJ*, 826, 56
- Riess A. G. et al., 2018, *ApJ*, 861, 126
- Rodríguez-Puebla A., Drory N., Avila-Reese V., 2012, *ApJ*, 756, 2
- Rodríguez-Puebla A., Avila-Reese V., Drory N., 2013, *ApJ*, 767, 92
- Rodríguez-Puebla A., Behroozi P., Primack J., Klypin A., Lee C., Hellinger D., 2016a, *MNRAS*, 462, 893
- Rodríguez-Puebla A., Primack J. R., Behroozi P., Faber S. M., 2016b, *MNRAS*, 455, 2592
- Rodríguez-Puebla A., Primack J. R., Avila-Reese V., Faber S. M., 2017, *MNRAS*, 470, 651
- Sahni V., Starobinsky A. A., 2000, *Int. J. Mod. Phys. D*, 9, 373
- Schaye J. et al., 2015, *MNRAS*, 446, 521
- Schmidt F., 2009, *Phys. Rev. D*, 80, 123003
- Shanks T., Hogarth L., Metcalfe N., 2019, *MNRAS*, 484, L64
- Sheth R. K., Connolly A. J., Kibba R., 2005, preprint (arXiv:astro-ph/0511773)
- Shi D., Li B., Han J., Gao L., Hellwing W. A., 2015, *MNRAS*, 452, 3179
- Shi D., Li B., Han J., 2017, *MNRAS*, 469, 705
- Shirasaki M., Hamana T., Yoshida N., 2015, *MNRAS*, 453, 3043
- Somerville R. S., Davé R., 2015, *ARA&A*, 53, 51
- Vainshtein A. I., 1972, *Phys. Lett. B*, 39, 393
- van den Bosch F., More S., Cacciato M., Mo H., Yang X., 2013, *MNRAS*, 430, 725
- Vikhlinin A. et al., 2009, *ApJ*, 692, 1060
- Vikram V., Cabré A., Jain B., VanderPlas J. T., 2013, *J. Cosmol. Astropart. Phys.*, 8, 020
- Vlah Z., White M., 2019, *JCAP*, 1903, 007
- Vogelsberger M. et al., 2014, *Nature*, 509, 177
- Wechsler R. H., Tinker J. L., 2018, *ARA&A*, 56, 435
- Weinberg S., 1989, *Rev. Mod. Phys.*, 61, 1
- White M., 2016, *J. Cosmol. Astropart. Phys.*, 1611, 057
- Will C. M., 2014, *Living Rev. Rel.*, 17, 4
- Winther H. A., Mota D. F., Li B., 2012, *ApJ*, 756, 166
- Yang X., Mo H. J., van den Bosch F. C., 2003, *MNRAS*, 339, 1057
- Yang X., Mo H. J., van den Bosch F. C., Pasquali A., Li C., Barden M., 2007, *ApJ*, 671, 153
- Yang X., Mo H. J., van den Bosch F. C., 2009, *ApJ*, 695, 900
- Yang X., Mo H. J., van den Bosch F. C., Zhang Y., Han J., 2012, *ApJ*, 752, 41
- Zehavi I. et al., 2011, *ApJ*, 736, 59
- Zhao G.-B., Li B., Koyama K., 2011, *Phys. Rev. Lett.*, 107, 071303

SUPPORTING INFORMATION

Supplementary data are available at *MNRAS* online.

Table D1. Central luminosity– V_{\max} relation from SHAM for all the models.

Table D2. Satellites luminosity– V_{\max} relation from SHAM for all the models.

Please note: Oxford University Press is not responsible for the content or functionality of any supporting materials supplied by the authors. Any queries (other than missing material) should be directed to the corresponding author for the article.

APPENDIX A: HALO MASS FUNCTIONS AND HALO CONCENTRATIONS FROM THE GRAVITY MODELS

The left-hand panel of Fig. A1 shows the halo mass function, $\phi_h(M_{200c})$, for all the gravity models employed in this paper. The bottom panel shows the relative differences with respect to the Λ CDM model. The trends noted for the halo velocity functions, Fig. 1, are similarly observed for the halo mass function, though the relative differences are of lower in amplitude for the latter. The right-hand panel of Fig. A1 shows the mean halo concentration–mass relation measured from the simulations corresponding to all the gravity models studied here. In the bottom panel, the relative

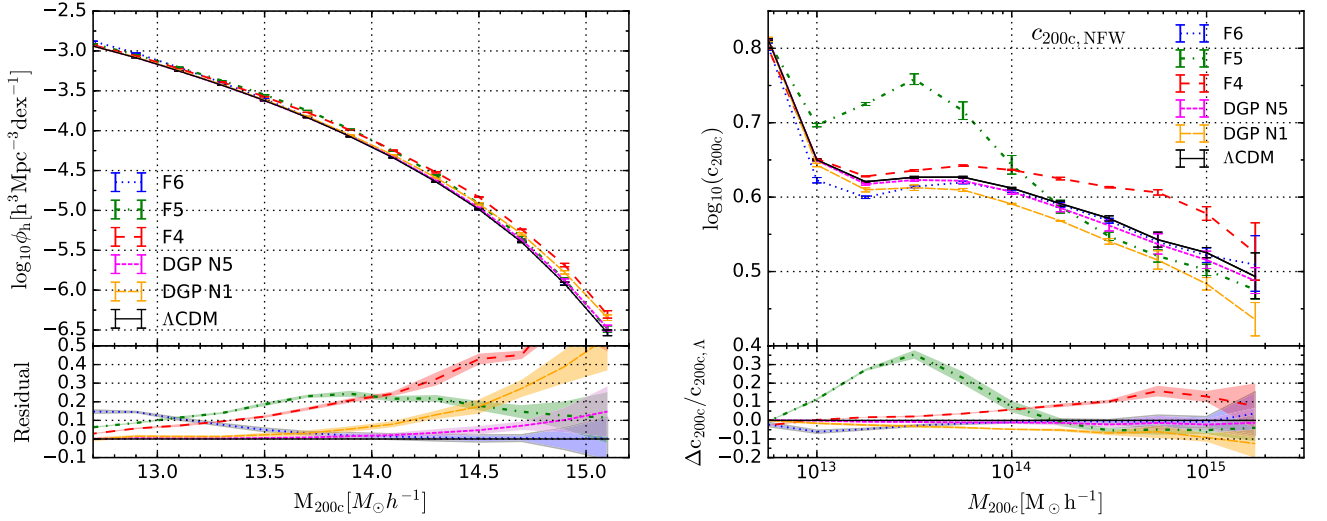


Figure A1. Left-hand panel: The differential halo mass M_{200c} function of the dark matter haloes for all the MG models including Λ CDM at redshift, $z = 0.0$. Right-hand panel: The dark matter halo concentrations as a function of M_{200c} at redshift $z = 0.0$. Their relative differences w.r.t. the Λ CDM is shown in their lower panels with the shade regions representing the error propagated from 1σ standard deviations of all the realizations. For this particular simulation resolution, F5 model is showing the highest deviation 20–25 per cent from Λ CDM in the mass ranges $10^{13.5} M_\odot h^{-1} < M_{200c} < 10^{14.5} M_\odot h^{-1}$ even larger deviation than F4, clearly showing the scales where the chameleon screening mechanism is inefficient for F5. F4 starts to deviate significantly from $10^{13.5} M_\odot h^{-1} < M_{200c}$ and continue to grow the deviation.

differences with respect to the Λ CDM model are shown. Note that the halo concentrations for the F5 model are significantly higher for masses $\sim 10^{13} - 10^{14} M_\odot h^{-1}$, the same mass range where the halo mass function presents an excess. Similarly, for the F4 model, the haloes become more and more concentrated than in Λ CDM for masses $\gtrsim 3 \times 10^{13} M_\odot h^{-1}$, the same mass range, where the halo mass function deviates significantly from the one of the Λ CDM model. Therefore, the respective haloes in these MG models are not only more abundant than in the Λ CDM model, but also more concentrated; the latter implies that for the same halo mass, V_{max} is higher in these MG models. As the result, the differences in the halo mass functions of the MG models with respect to the Λ CDM will further increase when plotting the halo V_{max} functions. The trends seen in Fig. A1 are mainly the result of the behaviour of the screening mechanisms, as discussed in Section 3.1.

APPENDIX B: THE IMPACT OF POISSONIAN ERROR

The cumulative GLFs for all the gravity models are presented in Fig. B1 along with their relative differences w.r.t. Λ CDM in the lower panel. This figure shows how accurately the SHAM technique has been applied to generate the mock galaxies catalogues irrespective of MG. One can notice from the lower panel of the figure that the noise level remains within 1 per cent until $M_r \sim -22.8$; afterward the Poissonian error becomes prominent. Hence, we mark this value as our threshold limit on M_r , beyond which our results can be biased by the Poissonian errors. Thus, the results we analysis below this limit $-22.8 > M_r - 5 \log h$ are marginal.

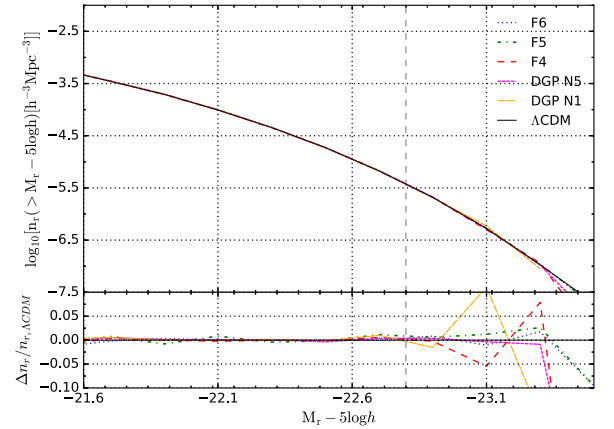


Figure B1. The cumulative $M_r - 5 \log h$ function of all type galaxies for all the models considered. The relative differences w.r.t. Λ CDM is shown in the lower panel. The dashed vertical line marks the threshold limit, below the threshold $M_r < -22.8$ the mock catalogues we generated using the SHAM technique can be biased by the Poisson noise of the cumulative function. This figure shows that the results we obtained within the ranges $-21.6 < M_r - 5 \log h < -22.8$ can be trust to understand the intrinsic effect of MG in our analysis.

APPENDIX C: LUMINOSITY FUNCTIONS FROM THE V_{max} FUNCTIONS AND $M_r - V_{\text{max}}$ RELATION

The GLFs of all models calculated using equation (31) under different density environments for one realization of the simulations

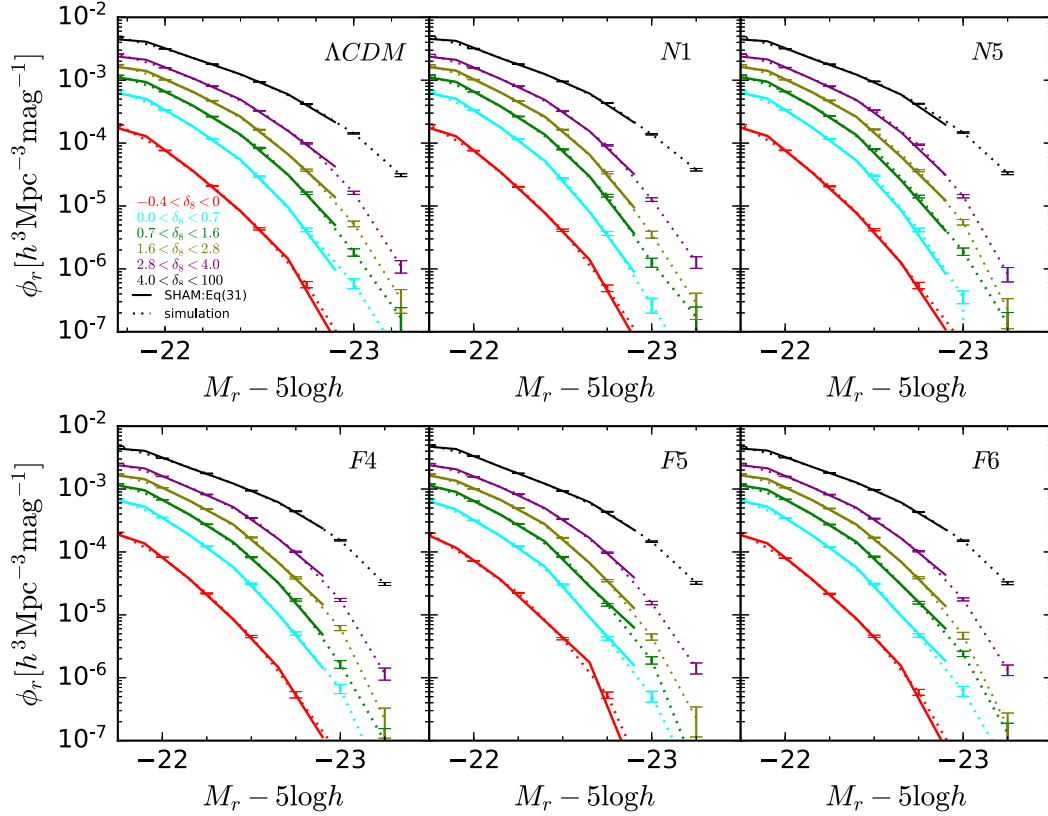


Figure C1. Comparison of the GLFs of all the models calculated using equation (31) (solid lines) with the one measured from our mock catalogues of galaxies (dotted lines) under six different density environments. The result is an outcome of one realization. Both are come out to consistent be with each other.

are shown in Fig. C1, presented as the solid lines in each panel. We also plot the corresponding GLFs measured from the simulation-based mock galaxy catalogues (dashed lines in the figures). As seen, the results are quite consistent with each other.

APPENDIX D: TABLES FOR THE M_r – V_{\max} RELATIONSHIPS SEPARATELY FOR CENTRALS AND SATELLITES

The M_r – V_{\max} relationships for central and satellite obtained from SHAM method separately for all the gravity models are provided as

supplementary. There we report the mean values for the realizations available for our suite of N -body simulations. Recall that r -band magnitudes were derived for a redshift rest frame of $z = 0$.

This paper has been typeset from a \LaTeX file prepared by the author.